Article

Abyssal ocean overturning slowdown and warming driven by Antarctic meltwater

https://doi.org/10.1038/s41586-023-05762-w

Received: 20 March 2022

Accepted: 25 January 2023

Published online: 29 March 2023

Check for updates

Qian Li[1], Matthew H. England[2]✉, Andrew McC. Hogg[3], Stephen R. Rintoul[4,5] & Adele K. Morrison[6]

The abyssal ocean circulation is a key component of the global meridional overturning circulation, cycling heat, carbon, oxygen and nutrients throughout the world ocean[1,2]. The strongest historical trend observed in the abyssal ocean is warming at high southern latitudes[2–4], yet it is unclear what processes have driven this warming, and whether this warming is linked to a slowdown in the ocean's overturning circulation. Furthermore, attributing change to specific drivers is difficult owing to limited measurements, and because coupled climate models exhibit biases in the region[5–7]. In addition, future change remains uncertain, with the latest coordinated climate model projections not accounting for dynamic ice-sheet melt. Here we use a transient forced high-resolution coupled ocean–sea-ice model to show that under a high-emissions scenario, abyssal warming is set to accelerate over the next 30 years. We find that meltwater input around Antarctica drives a contraction of Antarctic Bottom Water (AABW), opening a pathway that allows warm Circumpolar Deep Water greater access to the continental shelf. The reduction in AABW formation results in warming and ageing of the abyssal ocean, consistent with recent measurements. In contrast, projected wind and thermal forcing has little impact on the properties, age and volume of AABW. These results highlight the critical importance of Antarctic meltwater in setting the abyssal ocean overturning, with implications for global ocean biogeochemistry and climate that could last for centuries.

The Antarctic and Greenland ice sheets have lost mass at an accelerating rate over recent decades[8–11]. Future change in the melt rate of these ice sheets poses one of the most uncertain drivers of future change in the ocean, especially in relation to the ocean's overturning circulation, including both the upper-cell[12] and the abyssal ocean[13] circulation. Although extensive research has been undertaken to explore a possible slowdown of the Atlantic meridional overturning, little is known about the vulnerability of the Antarctic abyssal overturning circulation to climate change. The abyssal ocean is ventilated almost exclusively by cold, fresh and dense Antarctic Bottom Water (AABW) originating near the Antarctic continental margin and sinking along the continental slope to the ocean bottom[14,15]. Increased meltwater around Antarctica freshens the surface ocean and strengthens the stratification in regions where dense water is formed[16]. As such, changes in the Antarctic melt rate can change the ventilation rate of the abyssal ocean[13,17]. Ship-based measurements of repeated hydrographic sections between the 1990s and 2000s have detected significant warming and freshening in the ocean below 4,000 m, with the strongest trends around Antarctica[2–4]. Although recent progress has been made in understanding bottom water changes, because the abyssal ocean is both vast and challenging to observe, the physical mechanisms that govern these changes remain elusive.

Recent direct observations provide evidence that AABW has warmed, freshened and reduced in volume[18–23], although the drivers of these changes are not yet understood; they may reflect changes in the properties of Dense Shelf Water (DSW)[20,21], changes in the mixing ratio between DSW and Circumpolar Deep Water (CDW), or changes in circulation including a slowdown of the overturning. Incomplete observations of these processes around the Antarctic margin make it difficult to identify the cause. In addition, existing models have limitations for projecting AABW changes over the coming decades, owing to known baseline biases. Specifically, the latest Coupled Model Intercomparison Project Phase 6 (CMIP6)[24] models generally use a 1°-horizontal-resolution ocean component, in which the properties and formation rate of Antarctic Shelf Bottom Water and AABW are poorly represented[5], owing to unrealistic open-ocean deep convection[6]. Moreover, future climate change projections undertaken within CMIP6 do not incorporate ice-shelf and ice-sheet submodels, thus lacking a key component of the cryosphere system. In doing so, CMIP6 models either miss or underestimate the impact of additional meltwater on ocean circulation[25], which in turn underestimates future trends in AABW. Previous modelling work has examined the impact of meltwater changes on AABW formation[13,26–28]; however, these past studies all used models at coarse resolution, which is known to be insufficient to resolve ocean circulation and dense-water

[1]Department of Earth, Atmospheric, and Planetary Sciences, Massachusetts Institute of Technology, Cambridge, MA, USA. [2]Climate Change Research Centre and Australian Centre for Excellence in Antarctic Science, University of New South Wales, Sydney, New South Wales, Australia. [3]Research School of Earth Sciences and ARC Centre of Excellence for Climate Extremes, Australian National University, Canberra, Australian Capital Territory, Australia. [4]CSIRO Oceans & Atmosphere, Hobart, Tasmania, Australia. [5]Australian Antarctic Program Partnership, University of Tasmania, Hobart, Tasmania, Australia. [6]Research School of Earth Sciences and Australian Centre for Excellence in Antarctic Science, Australian National University, Canberra, Australian Capital Territory, Australia. ✉e-mail: M.England@unsw.edu.au

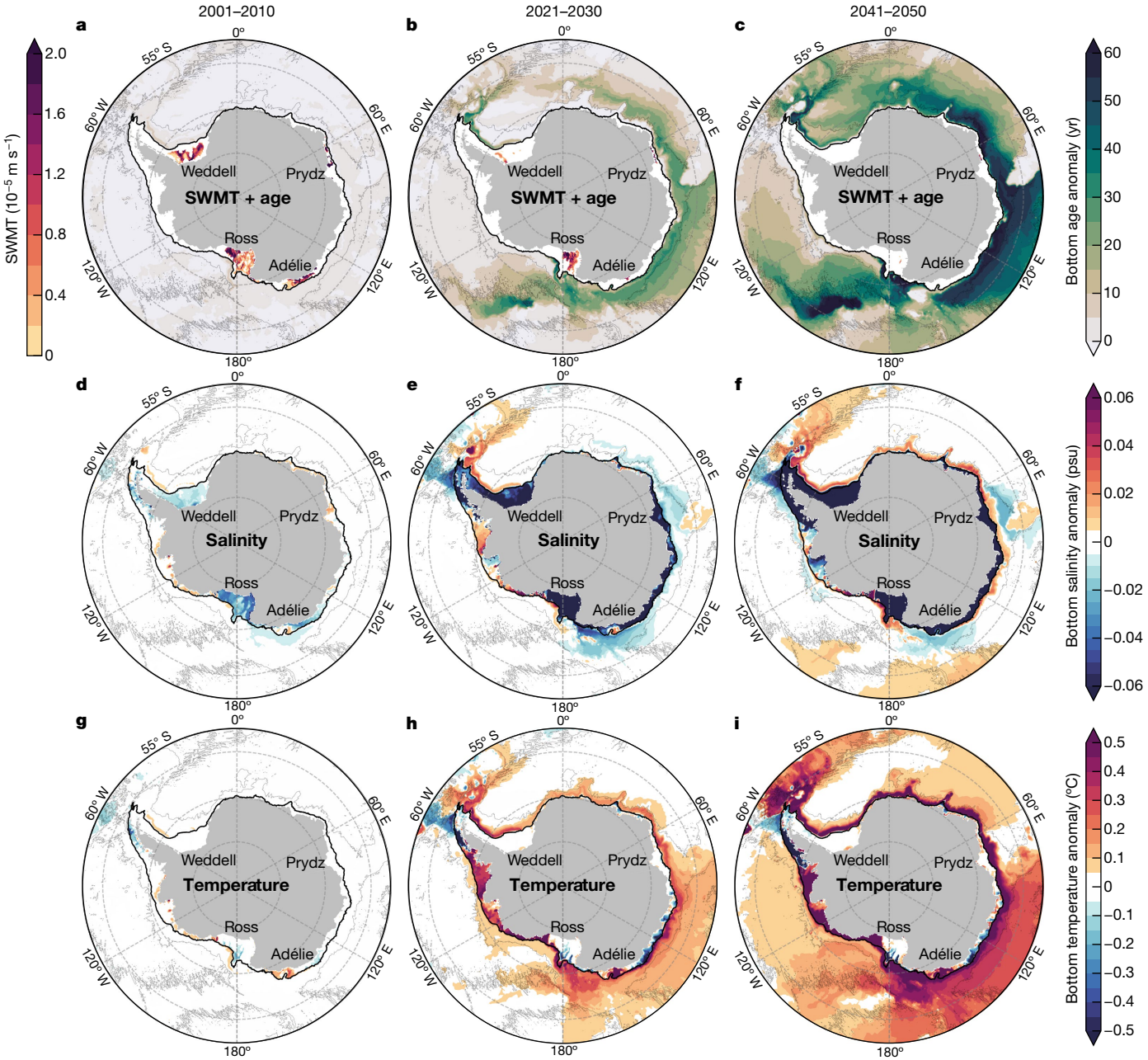

Fig. 1 | Recent and projected bottom water property changes from the main perturbation run. a–**i**, Surface water-mass transformation (SWMT; on the continental shelf) and bottom seawater age anomaly (in the abyss) (**a**–**c**), bottom salinity anomaly (**d**–**f**) and bottom temperature anomaly (**g**–**i**) from the [wind + thermal + meltwater] run during the decades 2001–2010 (**a**,**d**,**g**), 2021–2030 (**b**,**e**,**h**) and 2041–2050 (**c**,**f**,**i**) relative to the control run. The grey contours represent the 4,000-m isobath, and the black line denotes the 1,000-m isobath around the Antarctic margin. The SWMT rate is calculated across the 32.57 kg m^{-3} isopycnal (referenced to 1,000 m), across which the SWMT shows the most significant reduction.

formation over the Antarctic continental shelf, missing the required bathymetric features and resolution to capture downslope flows of dense-water plumes, and often forming AABW via open-ocean polynyas[5–7,28].

In this study, we assess how projected changes in meltwater, winds and surface warming will affect abyssal ventilation using a global ocean–sea-ice model that realistically captures AABW formation[29], the Antarctic continental shelf circulation[30], and the abyssal ocean circulation and hydrography[31] (Extended Data Figs. 1 and 2, and Methods). The model is spun-up for 200 years under repeat-year forcing before carrying out two experiments with globally perturbed forcing representing historical and projected climate changes in the zonal-mean fields of zonal winds, surface air temperature and longwave radiation, as well as Greenland and Antarctic ice-sheet melt. The historical wind, thermal and radiative perturbation forcing is based on observational products[32] for the historical period 1991–2019. The projected future perturbation forcing is derived from CMIP6 projections under a high-anthropogenic-emissions scenario for the period 2020–2050, with an additional meltwater perturbation forcing derived from an ice-sheet simulation[33] applied from 2001 to 2050 (Extended Data Fig. 3 and Methods). The first perturbation simulation is carried out with wind, thermal and meltwater anomalies, and the second with just wind and thermal anomalies. In this way, the contribution from the meltwater component to ongoing climate change can be estimated by analysing the difference between the two simulations. To account for model drift, we run a parallel control experiment using unperturbed forcing

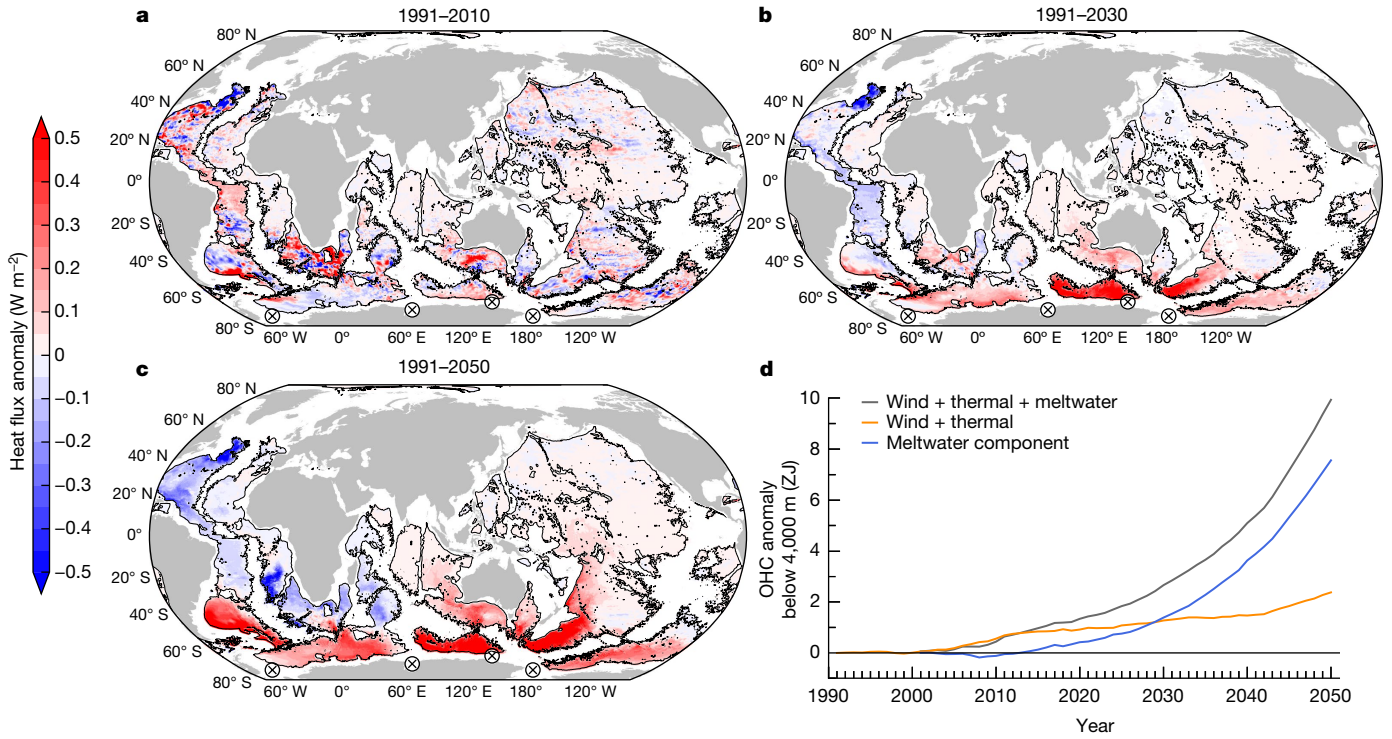

Fig. 2 | Recent and projected abyssal warming trends from the main perturbation run. a–**c**, Warming is shown as the heat flux anomaly across 4,000 m implied by the warming below 4,000 m during the periods 1991–2010 (**a**), 1991–2030 (**b**) and 1991–2050 (**c**) from the [wind + thermal + meltwater] run. The grey contours represent the 4,000-m isobath. The four arrow tail symbols along the coast of Antarctica denote the key locations of DSW and AABW formation. **d**, Time series of annual-mean globally integrated ocean heat content (OHC) anomaly below 4,000 m (ZJ = 10^{21} J) from the [wind + thermal + meltwater] run (grey line), the [wind + thermal] run (orange line), and the estimated meltwater component (blue line) derived from the difference between the two perturbation experiments with and without meltwater.

(Methods). It is noted that no coupled ocean or sea-ice feedbacks to the atmospheric forcing are included in the simulations, although a parallel coupled run with the same amount of added meltwater at coarse ocean model resolution[25] suggests that these feedbacks are weak around the Antarctic margin (Extended Data Fig. 4 and Methods). In addition, the sea-ice variations simulated in response to wind, thermal and meltwater anomalies are similar to that captured in fully coupled climate models (Extended Data Fig. 5 and Methods).

The high-resolution model we use[34] compares well to observed estimates of AABW formation and export[29], with plumes of DSW descending to the deep ocean from four primary sites on the continental shelf[35], namely the Ross Sea[36], Prydz Bay (Cape Darnley)[37], the Adélie Coast[38] and the Weddell Sea[39] (Extended Data Fig. 6a). In these locations, DSW is formed by atmospheric cooling and brine rejection during sea-ice growth. Dense water exported from the continental shelf descends the continental slope and mixes with lighter CDW to produce AABW[35]. Cold, fresh AABW then spreads northwards from the Antarctic margin to cover much of the global sea floor[14]. These abyssal waters eventually recirculate back to the upper ocean, enriched in nutrients and carbon sourced at depth, thus regulating ocean biological production and the global carbon cycle via export productivity and carbon dioxide outgassing[40,41].

Abyssal ocean response

The response of the abyssal ocean to the projected climate anomalies is now examined. Abyssal ventilation is closely tied to the production rate of cold and salty DSW, which is controlled by surface buoyancy fluxes along the Antarctic continental margins[42]. On the basis of a surface water-mass transformation approach[43] (Methods), we estimate the control experiment DSW formation rate to be 7.26 Sv (1 Sv = 10^6 m^3 s^{-1}) formed across the 32.57 kg m^{-3} isopycnal (Extended Data Fig. 6b), which compares reasonably well with the volume transport of ventilated AABW (8.1 Sv, of which 5.4 ± 1.7 Sv is DSW; as estimated by ref. [44]). As the projected meltwater continues to be added to 2050, progressive freshening drives a significant decline in the formation rate of DSW, with the most significantly reduced surface water-mass transformation occurring across the 32.57 kg m^{-3} density surface (Extended Data Fig. 6c–e).

Figure 1 illustrates the distribution of bottom water property changes during the historical and future periods under wind, thermal and meltwater forcing perturbations. The meltwater forcing drives the majority of these bottom water changes (Extended Data Fig. 7). During the decade 2001–2010, the freshening rate on the continental shelf is about 0.03 psu per decade in the Ross Sea (Fig. 1d), which is consistent with observational studies of recent trends[19,20]. The change in the production rate of DSW via surface water-mass transformation during this period is small (Fig. 1a and Extended Data Fig. 6a) and has little impact on bottom water properties (Fig. 1a,d,g). In contrast, by 2041–2050, the accumulation of fresh water owing to ice-sheet melt reduces the production rate of DSW, with the surface water-mass transformation decreasing to nearly zero across the 32.57 kg m^{-3} isopycnal (Fig. 1c). Following the spreading pathways of AABW, the abyssal ocean becomes warmer and less ventilated (indicated by increasing age), with the strongest signal of change (that is, more than 0.2 °C of warming) in the Australian–Antarctic Basin (Fig. 1c,i). Positive salinity anomalies also start to appear on the continental slope within a narrow band circling Antarctica during 2041–2050 (Fig. 1f).

The model simulates the historical trends in heat and freshwater fluxes across 4,000 m with a pattern and magnitude that agree reasonably well with observations on a large basin scale, particularly the circumpolar warming trend that has developed across the abyssal Southern Ocean during recent decades[2,3,45] (Methods). The abyssal warming signal initiates near the formation sites of AABW and extends northwards along the export pathways of AABW[46,47]. By comparing

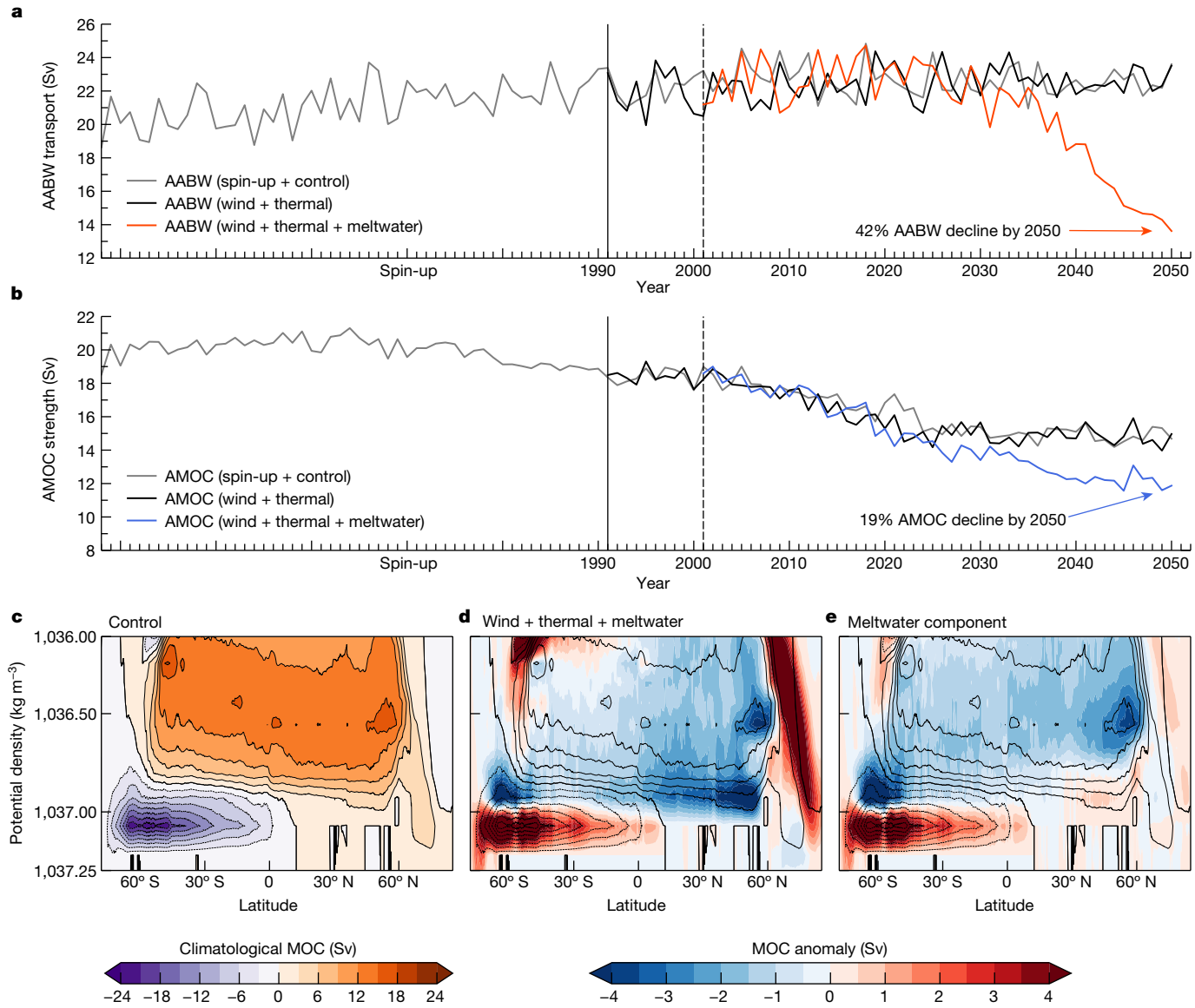

Fig. 3 | Projected global overturning circulation changes out to 2050. **a**,**b**, Time series of annual-mean AABW transport (**a**) and AMOC strength (**b**) from the spin-up and control run (grey line), the [wind + thermal] run (black line) and the [wind + thermal + meltwater] run (orange and blue lines). **c**, Climatological mean meridional overturning circulation (MOC) from the control run. **d**,**e**, MOC anomaly during 2041–2050 from the [wind + thermal + meltwater] run (**d**) and the meltwater component (**e**). Contours in **c**–**e** represent the climatological mean MOC with an interval of 3 Sv and the 0-Sv line in bold. All MOC values are calculated in density coordinates. The AABW transport is defined as the maximum magnitude of the overturning streamfunction in density coordinates between 40° S and 50° S, and below the density level 1,036.8 kg m^{-3}. The AMOC strength is defined as the maximum overturning streamfunction at 45° N. Percentage decline values shown in **a** and **b** indicate the percentage reduction in the MOC indices relative to the control run.

the perturbation runs with and without meltwater, we can see that the warming of AABW is largely driven by meltwater (Extended Data Fig. 8). The fastest abyssal warming takes place in the Australian–Antarctic Basin, where the increase in heat content below 4,000 m between 1991 and 2030 corresponds to a basin-averaged heat flux of more than 0.5 W m^{-2}. By 2050, the abyssal warming is projected to continue at an increasing rate and to spread more broadly through all Southern Ocean basins (Fig. 2c). The simulations project that meltwater forcing will dominate future increases in globally integrated abyssal ocean heat content after 2030, much larger than the projected wind and warming effects (Fig. 2d).

Although the warming of AABW is predominantly driven by Antarctic meltwater, the evolution of freshwater content below 4,000 m is controlled by all three forcing perturbations (Extended Data Fig. 9). In particular, the wind and thermal forcing drives an overall abyssal freshening around Antarctica, including in the Australian–Antarctic, Weddell–Enderby and Amundsen–Bellingshausen basins (Extended Data Fig. 9d–f). This freshening is possibly associated with an increase in sea-ice melt due to the warming anomalies in that experiment (Extended Data Fig. 10). In contrast, the meltwater forcing initially also drives abyssal freshening, but then there is a reversal towards more saline abyssal waters, particularly in the Australian–Antarctic and Amundsen–Bellingshausen basins (Extended Data Fig. 9g–i), due to changes in circulation such as the contraction of AABW and poleward displacement of CDW (discussed in more detail below). It is noted that our experiments cannot simulate any observed abyssal salinity variations that are forced by intrinsic interannual-to-multidecadal atmospheric variability. Instead, the experiments are designed to examine long-term climate-change-forced anomalies in the ocean abyss (Methods).

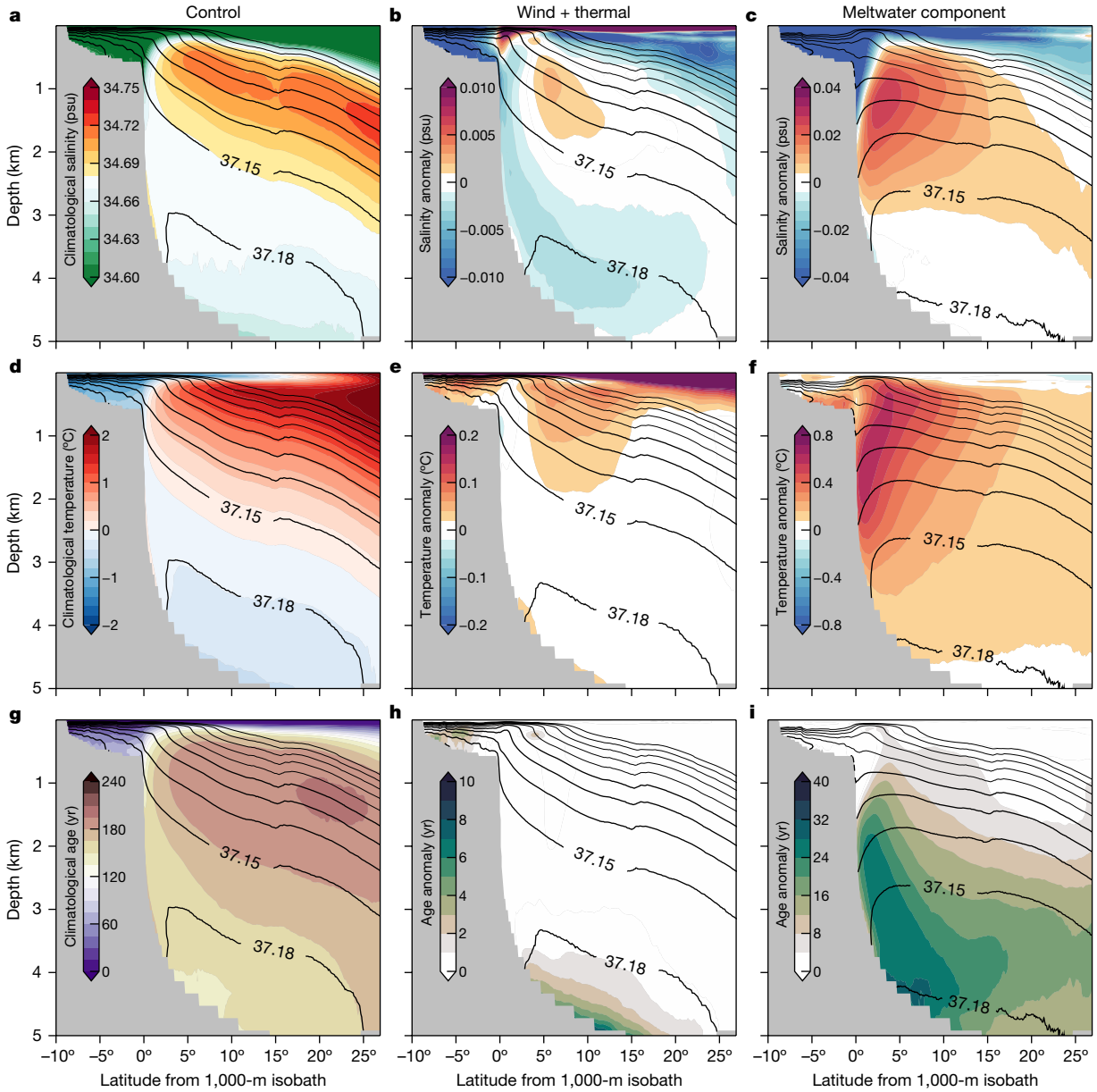

Fig. 4 | Projected Southern Ocean water-mass changes in 2041–2050. **a**–**i**, Vertical cross-sections of zonal-mean salinity (**a**–**c**), temperature (**d**–**f**) and seawater age (**g**–**i**) during 2041–2050 from the control run (climatology; **a**,**d**,**g**), the [wind + thermal] run (anomaly; **b**,**e**,**h**) and the meltwater component (anomaly; **c**,**f**,**i**). The meltwater component is estimated from the difference between the [wind + thermal + meltwater] run and the [wind + thermal] run. Contours show the corresponding potential density (referenced to 2,000 m) during 2041–2050, ranging from 36.91 kg m^{-3} to 37.18 kg m^{-3} with an interval of 0.03 kg m^{-3}. Latitude is shown relative to the 1,000-m isobath. Note that different colour-map scales are applied for anomalies from the [wind + thermal] run (**b**,**e**,**h**) and the meltwater component (**c**,**f**,**i**).

Global overturning circulation response

The perturbation experiments show that the global overturning circulation, which drives the interbasin exchange of heat, salt, dissolved gases and nutrients[48], is expected to weaken in response to projected changes in forcing. As shown in Fig. 3c, the control climate overturning circulation includes two global-scale meridional overturning cells: namely, an upper cell linked to the Atlantic Meridional Overturning Circulation (AMOC), and a lower cell driven by AABW formation and export[49]. Here we define the AABW transport as the maximum magnitude of the overturning streamfunction in density coordinates between 40° S and 50° S, and below the density level 1,036.8 kg m^{-3}. The AMOC strength is defined as the maximum overturning streamfunction at 45° N. As the meltwater release from Greenland and Antarctica increases over time, the AABW overturning and AMOC strength both weaken by 2050 (Fig. 3a,b). The strength of the AABW overturning cell and the AMOC is projected to decrease by 42% (10.0 Sv) and 19% (2.8 Sv) by 2050, respectively. Meltwater forcing drives virtually all of the reduction in overturning in the AABW cell (Fig. 3d,e), with seawater ageing along the pathway of AABW outflow (Extended Data Fig. 11). The projected decline of AMOC results in reduced northward ocean heat transport[50], leading to a cooling trend in the abyssal Atlantic Ocean (Fig. 2). In contrast, the projected decline of AABW drives a warming trend across the abyssal Southern Ocean (Fig. 2), reminiscent in structure to recently observed bottom water trends[2,3].

Mechanisms for reduced abyssal overturn

Changes in AABW, which is comprised of a mixture of DSW, CDW and Antarctic Surface Water, could reflect changes in these end-members or in the mixing between them. Vertical cross-sections provide some

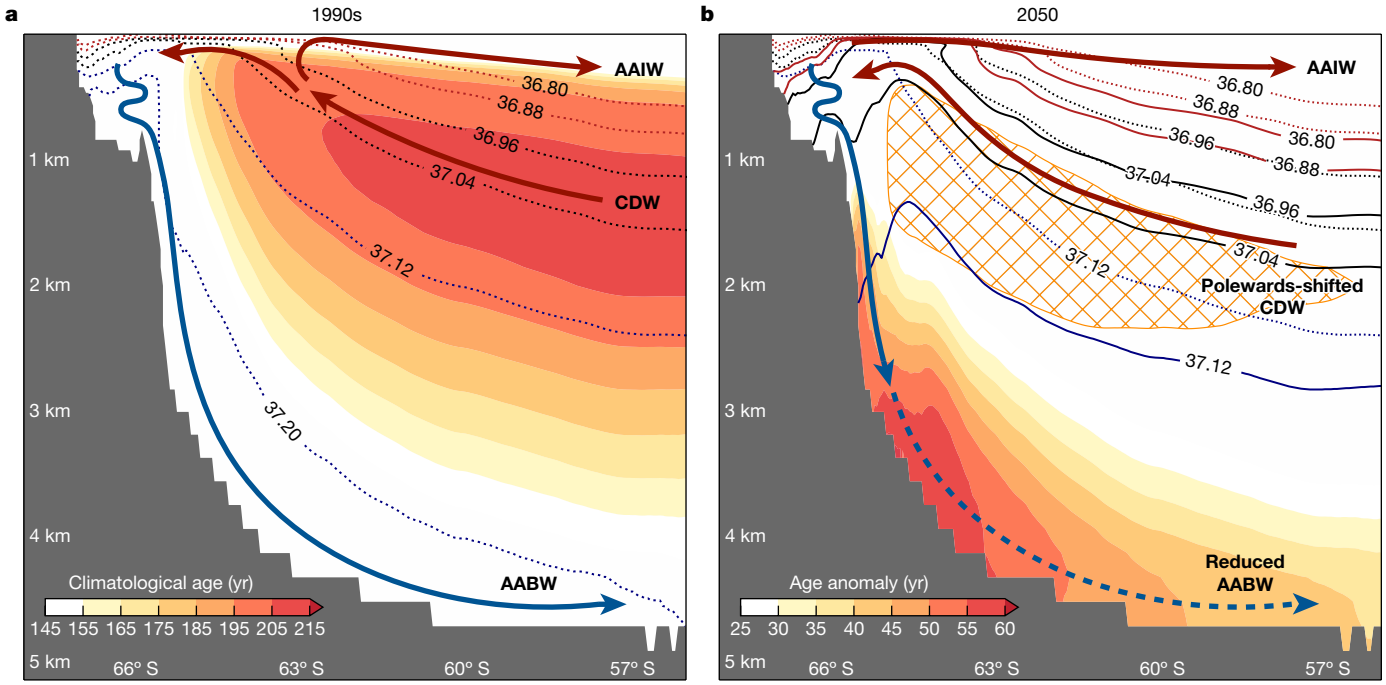

Fig. 5 | Schematic showing mechanisms for reduced abyssal ventilation in 2050. a,**b**, Vertical cross-sections of zonal-mean climatological mean seawater age (colour) in the 1990s from the control run (**a**) and seawater age anomaly (colour) and salinity anomaly (hatched) in 2050 from the [wind + thermal + meltwater] run (**b**), relative to the control, for an AABW formation sector near the Adélie Coast (120° E–130° E). The hatched area in **b** denotes a positive salinity anomaly of >0.025 psu. The dotted contours in both panels show potential density surfaces (referenced to 2,000 m) in the control run, with values ranging from 36.80 kg m^{-3} to 37.20 kg m^{-3} with an interval of 0.08 kg m^{-3}; solid contours in **b** show the same potential density surfaces in the [wind + thermal + meltwater] run. Note that in **b**, the control run density surfaces in **a** are only shown if that density surface is still present in 2050 (hence there is no 37.20 kg m^{-3} surface indicated in **b**). The red arrows denote CDW upwelling towards the sea surface in **a** and moving onto the continental slope in **b**, with surface waters flowing northwards to form Antarctic Intermediate Water (AAIW). The blue arrows represent the climatological mean AABW in **a** and the projected contraction of AABW in **b**.

insight into the physical mechanisms regulating abyssal ventilation in the two perturbation experiments (Fig. 4). In the control run, the CDW that shoals along isopycnals to reach the base of the surface mixed layer is relatively warm (1.5 °C), saline (34.70–34.75 psu) and old. The extension of CDW southwards towards the upper continental slope generates a sharp front between warm, saline and old CDW, and cold, fresh and young shelf water (Fig. 4a,d,g). Onshore CDW intrusion can be identified as relatively warm saline waters being transported across the shelf break; this is a critical process controlling basal melt of the ice shelves[51–53].

The wind and thermal forcing experiment drives significant changes in the upper ocean, but only small changes in the deep ocean. Specifically, this experiment reveals an anomalous freshening on the shelf and in the upper ocean (Fig. 4b), probably due to enhanced sea-ice melt (Extended Data Fig. 10). Some of the fresher shelf water cascades off the shelf and reaches the abyss, causing weak freshening of AABW (Fig. 4b), but little change in the strength of the AABW overturning cell (Fig. 3a). Other than that, there is only weak warming in CDW offshore (Fig. 4e), a small increase in age of AABW (Fig. 4h), and little change in isopycnals and overturning (Extended Data Fig. 12c) relative to the control run (Extended Data Fig. 12a).

In contrast, the meltwater forcing drives marked changes over the continental shelf, slope and rise. First, freshening of shelf waters extends down the slope and offshore (Fig. 4c). Salinity increases over the upper continental slope (1,000–3,000 m depth), with the strongest signal at the southern limit of CDW, reflecting poleward displacement of CDW (Fig. 4c). The poleward shift of CDW also causes warming, with the strongest signal over the upper continental slope and weaker warming throughout the water column at other locations (Fig. 4f). Shelf waters freshen but with little change in temperature (Fig. 4c,f). Furthermore, the abyssal overturning and ventilation are significantly reduced, resulting in a notable increase in abyssal age (Fig. 4i). Changes in isopycnals are also evident over the continental slope and in the deep ocean. For instance, in the control run, the 37.15 kg m^{-3} isopycnal intersects the continental shelf break above 600 m depth (Extended Data Fig. 12a); with meltwater forcing, this isopycnal intersects the continental slope below 3,000 m depth (Extended Data Fig. 12d). It is noted that changes in temperature and salinity on depth levels can reflect either adiabatic movement of isopycnal surfaces, or changes in water-mass properties due to mixing or buoyancy fluxes. Using the framework of density coordinate transformation (Methods), we are able to distinguish between these two components. In fact, they largely compensate each other above about 1,000 m (Extended Data Fig. 13). Below 1,000 m depth, the warming and salinification over the Antarctic continental slope are primarily caused by descent of isopycnals (Extended Data Fig. 13b,e), referred to as 'heaving' of the water column[54]. As isopycnals descend, both temperature and salinity increase on pressure surfaces from the AABW layer up to the salinity maximum core of CDW. When examining water-mass changes once the effects of isopycnal heave have been removed, it is apparent that the fresher DSW and weaker overturning circulation lead to a freshening in the AABW layer (Extended Data Fig. 13c).

The physical mechanisms that drive the abyssal ocean changes are summarized in Fig. 5. First, the projected addition of Antarctic meltwater causes an anomalous freshening of DSW, which produces fresher and less dense AABW, and eventually reduced AABW volume, after the 2030s. Disappearance of the densest classes of AABW and a slowdown in the sinking of AABW cause isopycnals to deepen, with the strongest signal evident over the slope where the decrease in thickness of the AABW layer is largest. The primary cause of these changes is heave (descent of isopycnals), rather than water-mass transformation

by surface buoyancy forcing and transport of anomalies from shallow to deep depths. Descent of isopycnals allows relatively warm and salty CDW to spread polewards and downwards, so that dense AABW is replaced by lighter AABW and CDW. A reduction in the volume of DSW combined with mixing with older CDW over the slope results in weakened ventilation and seawater ageing along the pathway of AABW outflow. In fact, the meltwater input does not ultimately freshen AABW on the continental slope (Fig. 4c), because the salinity increase at depth arising from heave more than compensates for the fresher shelf water that is carried to depth by the weaker overturning circulation. Because the isopycnal heaving and the slowdown in AABW formation and export both contribute to the age increase at depth, the age anomaly extends deeper and farther offshore than the temperature and salinity anomalies (Extended Data Fig. 13g–i).

We have shown that projected increases in Antarctic ice melt are set to drive a substantial slowdown of the lower cell of the global overturning circulation over the coming decades, resulting in large and widespread warming of deep waters and reduced ventilation of the abyssal ocean. In particular, a net slowdown of the abyssal ocean overturning circulation of just over 40% is projected to occur by 2050. These changes in the lower cell would profoundly alter the ocean overturning of heat, fresh water, oxygen, carbon and nutrients, with impacts felt throughout the global ocean for centuries to come.

Online content

Any methods, additional references, Nature Portfolio reporting summaries, source data, extended data, supplementary information, acknowledgements, peer review information; details of author contributions and competing interests; and statements of data and code availability are available at https://doi.org/10.1038/s41586-023-05762-w.

1. Purkey, S. G. et al. A synoptic view of the ventilation and circulation of Antarctic Bottom Water from chlorofluorocarbons and natural tracers. *Annu. Rev. Mar. Sci.* **10**, 503–527 (2018).
2. Purkey, S. G. & Johnson, G. C. Warming of global abyssal and deep Southern Ocean waters between the 1990s and 2000s: contributions to global heat and sea level rise budgets. *J. Clim.* **23**, 6336–6351 (2010).
3. Purkey, S. G. & Johnson, G. C. Antarctic Bottom Water warming and freshening: contributions to sea level rise, ocean freshwater budgets, and global heat gain. *J. Clim.* **26**, 6105–6122 (2013).
4. Desbruyères, D. G., Purkey, S. G., McDonagh, E. L., Johnson, G. C. & King, B. A. Deep and abyssal ocean warming from 35 years of repeat hydrography. *Geophys. Res. Lett.* **43**, 10356–10365 (2016).
5. Purich, A. & England, M. H. Historical and future projected warming of Antarctic Shelf Bottom Water in CMIP6 models. *Geophys. Res. Lett.* **48**, e2021GL092752 (2021).
6. Heuzé, C. Antarctic Bottom Water and North Atlantic Deep Water in CMIP6 models. *Ocean Sci.* **17**, 59–90 (2021).
7. Heuzé, C., Heywood, K. J., Stevens, D. P. & Ridley, J. K. Changes in global ocean bottom properties and volume transports in CMIP5 models under climate change scenarios. *J. Clim.* **28**, 2917–2944 (2015).
8. Paolo, F. S., Fricker, H. A. & Padman, L. Volume loss from Antarctic ice shelves is accelerating. *Science* **348**, 327–331 (2015).
9. The IMBIE team Mass balance of the Antarctic Ice Sheet from 1992 to 2017. *Nature* **558**, 219–222 (2018).
10. The IMBIE team Mass balance of the Greenland Ice Sheet from 1992 to 2018. *Nature* **579**, 233–239 (2020).
11. Stokes, C. R. et al. Response of the East Antarctic Ice Sheet to past and future climate change. *Nature* **608**, 275–286 (2022).
12. Lohmann, J. & Ditlevsen, P. D. Risk of tipping the overturning circulation due to increasing rates of ice melt. *Proc. Natl Acad. Sci. USA* **118**, e2017989118 (2021).
13. Lago, V. & England, M. H. Projected slowdown of Antarctic Bottom Water formation in response to amplified meltwater contributions. *J. Clim.* **32**, 6319–6335 (2019).
14. Orsi, A. H., Jacobs, S. S., Gordon, A. L. & Visbeck, M. Cooling and ventilating the abyssal ocean. *Geophys. Res. Lett.* **28**, 2923–2926 (2001).
15. Johnson, G. C. Quantifying Antarctic Bottom Water and North Atlantic Deep Water volumes. *J. Geophys. Res. Oceans* **113**, C05027 (2008).
16. Moorman, R., Morrison, A. K. & Hogg, A. M. Thermal responses to Antarctic Ice Shelf melt in an eddy-rich global ocean–sea ice model. *J. Clim.* **33**, 6599–6620 (2020).
17. Bronselaer, B. et al. Importance of wind and meltwater for observed chemical and physical changes in the Southern Ocean. *Nat. Geosci.* **13**, 35–42 (2020).
18. Rintoul, S. R. Rapid freshening of Antarctic Bottom Water formed in the Indian and Pacific oceans. *Geophys. Res. Lett.* **34**, L06606 (2007).
19. Jacobs, S. S. & Giulivi, C. F. Large multidecadal salinity trends near the Pacific–Antarctic continental margin. *J. Clim.* **23**, 4508–4524 (2010).
20. van Wijk, E. M. & Rintoul, S. R. Freshening drives contraction of Antarctic Bottom Water in the Australian Antarctic Basin. *Geophys. Res. Lett.* **41**, 1657–1664 (2014).
21. Purkey, S. G. & Johnson, G. C. Global contraction of Antarctic Bottom Water between the 1980s and 2000s. *J. Clim.* **25**, 5830–5844 (2012).
22. Aoki, S. et al. Reversal of freshening trend of Antarctic Bottom Water in the Australian–Antarctic Basin during 2010s. *Sci. Rep.* **10**, 14415 (2020).
23. Silvano, A. et al. Recent recovery of Antarctic Bottom Water formation in the Ross Sea driven by climate anomalies. *Nat. Geosci.***13**, 780–786 (2020).
24. Eyring, V. et al. Overview of the Coupled Model Intercomparison Project Phase 6 (CMIP6) experimental design and organization. *Geosci. Model Dev.* **9**, 1937–1958 (2016).
25. Purich, A. & England, M. H. Projected impacts of Antarctic meltwater anomalies over the 21st century. *J. Clim.* **36**, 2703–2719 (2023).
26. Mikolajewicz, U. Effect of meltwater input from the Antarctic Ice Sheet on the thermohaline circulation. *Ann. Glaciol.* **27**, 311–315 (1998).
27. Fogwill, C. J., Phipps, S. J., Turney, C. S. M. & Golledge, N. R. Sensitivity of the Southern Ocean to enhanced regional Antarctic Ice Sheet meltwater input. *Earths Future* **3**, 317–329 (2015).
28. Jeong, H. et al. Impacts of ice-shelf melting on water-mass transformation in the Southern Ocean from E3SM simulations. *J. Clim.* **33**, 5787–5807 (2020).
29. Morrison, A. K., Hogg, A. M., England, M. H. & Spence, P. Warm Circumpolar Deep Water transport toward Antarctica driven by local dense water export in canyons. *Sci. Adv.* **6**, eaav2516 (2020).
30. Huneke, W. G. C., Morrison, A. K. & Hogg, A. M. Spatial and subannual variability of the Antarctic Slope Current in an eddying ocean–sea ice model. *J. Phys. Oceanogr.* **52**, 347–361 (2022).
31. Solodoch, A. et al. How does Antarctic Bottom Water cross the Southern Ocean? *Geophys. Res. Lett.* **49**, e2021GL097211 (2022).
32. Tsujino, H. et al. JRA-55 based surface dataset for driving ocean-sea-ice models (JRA55-do). *Ocean Model.* **130**, 79–139 (2018).
33. Golledge, N. R. et al. Global environmental consequences of twenty-first-century ice-sheet melt. *Nature* **566**, 65–72 (2019).
34. Kiss, A. E. et al. ACCESS-OM2 v1.0: a global ocean–sea ice model at three resolutions. *Geosci. Model Dev.* **13**, 401–442 (2020).
35. Baines, P.G. & Condie, S. Observations and modelling of Antarctic downslope flows: A review. In *Ocean, Ice, and Atmosphere: Interactions at the Antarctic Continental Margin* (eds Jacobs, S. S & Weiss, R. F.) 29–49 (American Geophysical Union, 1985).
36. Gordon, A. L. et al. Energetic plumes over the western Ross Sea continental slope. *Geophys. Res. Lett.* **31**, L21302 (2004).
37. Ohshima, K. I. et al. Antarctic Bottom Water production by intense sea-ice formation in the Cape Darnley polynya. *Nat. Geosci.* **6**, 235–240 (2013).
38. Williams, G. D. et al. Antarctic Bottom Water from the Adélie and George V Land coast, East Antarctica (140–149°E). *J. Geophys. Res. Oceans* **115**, C04027 (2010).
39. Nicholls, K. W., Østerhus, S., Makinson, K., Gammelsrød, T. & Fahrbach, E. Ice–ocean processes over the continental shelf of the southern Weddell Sea, Antarctica: a review. *Rev. Geophys.* **47,** RG3003 (2009).
40. Marinov, I., Gnanadesikan, A., Toggweiler, J. R. & Sarmiento, J. L. The Southern Ocean biogeochemical divide. *Nature* **441**, 964–967 (2006).
41. Liu, Y., Moore, J. K., Primeau, F. & Wang, W. L. Reduced CO_2 uptake and growing nutrient sequestration from slowing overturning circulation. *Nat. Clim. Change* **13**, 83–90 (2023).
42. Snow, K., Hogg, A. M., Sloyan, B. M. & Downes, S. M. Sensitivity of Antarctic Bottom Water to changes in surface buoyancy fluxes. *J. Clim.* **29**, 313–330 (2016).
43. Abernathey, R. P. et al. Water-mass transformation by sea ice in the upper branch of the Southern Ocean overturning. *Nat. Geosci.* **9**, 596–601 (2016).
44. Orsi, A. H., Smethie Jr, W. M. & Bullister, J. L. On the total input of Antarctic waters to the deep ocean: a preliminary estimate from chlorofluorocarbon measurements. *J. Geophys. Res. Oceans* **107**, 31-1–31-14 (2002).
45. Bindoff, N. L. et al. in *IPCC Special Report on the Ocean and Cryosphere in a Changing Climate* (eds Pörtner, H.-O. et al.) Ch. 5, 447–587 (Cambridge Univ. Press, 2019).
46. Sen Gupta, A. & England, M. H. Evaluation of interior circulation in a high-resolution global ocean model. Part I: deep and bottom waters. *J. Phys. Oceanogr.* **34**, 2592–2614 (2004).
47. Kusahara, K., Williams, G. D., Tamura, T., Massom, R. & Hasumi, H. Dense shelf water spreading from Antarctic coastal polynyas to the deep Southern Ocean: a regional circumpolar model study. *J. Geophys. Res. Oceans* **122**, 6238–6253 (2017).
48. Talley, L. D. Closure of the global overturning circulation through the Indian, Pacific, and Southern oceans: schematics and transports. *Oceanography* **26**, 80–97 (2013).
49. Marshall, J. & Speer, K. Closure of the meridional overturning circulation through Southern Ocean upwelling. *Nat. Geosci.* **5**, 171–180 (2012).
50. Manabe, S. & Stouffer, R. J. Coupled ocean–atmosphere model response to freshwater input: comparison to Younger Dryas Event. *Paleoceanography* **12**, 321–336 (1997).
51. Pritchard, H. D. et al. Antarctic ice-sheet loss driven by basal melting of ice shelves. *Nature* **484**, 502–505 (2012).
52. Rintoul, S. R. et al. Ocean heat drives rapid basal melt of the Totten Ice Shelf. *Sci. Adv.* **2**, e1601610 (2016).
53. Bronselaer, B. et al. Change in future climate due to Antarctic meltwater. *Nature* **564**, 53–58 (2018).
54. Bindoff, N. L. & Mcdougall, T. J. Diagnosing climate change and ocean ventilation using hydrographic data. *J. Phys. Oceanogr.* **24**, 1137–1152 (1994).

Publisher's note Springer Nature remains neutral with regard to jurisdictional claims in published maps and institutional affiliations.

Springer Nature or its licensor (e.g. a society or other partner) holds exclusive rights to this article under a publishing agreement with the author(s) or other rightsholder(s); author self-archiving of the accepted manuscript version of this article is solely governed by the terms of such publishing agreement and applicable law.

© The Author(s), under exclusive licence to Springer Nature Limited 2023

Methods

Global ocean–sea-ice model

This study uses the Australian Community Climate and Earth System Simulator Ocean Model version 2 (ACCESS-OM2) with the configuration at nominally 0.1° horizontal resolution (ACCESS-OM2-01). ACCESS-OM2 is a global ocean–sea-ice model driven by a prescribed atmosphere[34]. The ocean model component is the Modular Ocean Model Version 5.1 (MOM5.1)[55], coupled to the Los Alamos sea-ice model version 5.1.2 (CICE5.1.2)[56]. ACCESS-OM2 uses a tripolar grid with one pole located at the South Pole and the other two poles located over land north of 65° N, and a Mercator projection down to 65° S. South of 65° S, the meridional grid spacing is held at the same value (in km) as 65° S. The model configuration employs a z^* generalized vertical coordinate with partial cells, and includes the boundary-layer K-profile parameterization (KPP)[57] with a constant background vertical viscosity of 10^{-4} m^2 s^{-1}. The surface salinity restoring is applied globally to limit errors that can result in simulated ocean properties and circulation[58], with the strength set by the piston velocity or Newtonian damping rate of 50 m per 450 days[34]. This restoring is weak enough to allow a response to the prescribed meltwater anomalies, while also maintaining a realistic control ocean simulation state.

For the high-resolution ACCESS-OM2-01 used here, the median zonal cell size is about 7.2 km globally. In the Southern Ocean, the horizontal resolution ranges from 9 km at 36° S to 4 km at 68° S, hence it is eddy-permitting in much of this region where it resolves the largest baroclinic mesoscale eddies. The model uses a 75-level vertical grid with grid spacing from 1.1 m at the surface to 198.4 m at the bottom-most grid cells at 5,808.7 m. There is no subgrid-scale parameterization for mesoscale eddies included in the simulations. A parameterization for restratification in the mixed layer owing to submesoscale eddies is applied[59]. For Antarctica, with no resolved ice-shelf cavities, the approximately equal magnitude of climatological mean iceberg calving and ice-shelf basal melt is deposited as liquid run-off (via virtual salt fluxes) at the coast in the upper 40 m of the ocean in our model[32], as provided in ref. [60]. The model has no explicit tides, but bottom-enhanced internal tidal mixing[61] and barotropic tidal mixing[62] are both parameterized. Nevertheless, the model is able to accurately represent AABW formation[29] and the Antarctic continental shelf circulation[30], with localized DSW formation appearing over the continental shelf in four distinct sectors (that is, the Ross Sea[36], Prydz Bay (Cape Darnley)[37], the Adélie Coast[38] and the Weddell Sea[39]), as also seen in observations. The high-resolution ocean model used here also reproduces abyssal ocean circulation and hydrography with much greater accuracy compared with CMIP6 simulations, even when considering the CMIP6 multi-model mean that typically averages out biases across different models (Extended Data Figs. 1 and 2).

Experimental design

The model is first spun-up for 200 years using the May 1990–April 1991 repeat-year forcing[63] based on the Japanese 55-year Reanalysis (JRA55) dataset for driving ocean–sea-ice models version 1.3 (JRA55-do v1.3)[32]. From the spun-up state, we conduct a parallel control climate run, alongside two sets of perturbation experiments to study the ocean's response to different forcing components under climate change. These two simulations use the same repeat-year forcing except for the components that are perturbed. The main perturbation experiment comprises anomalous wind, thermal and meltwater forcing, whereas the second perturbation run comprises just anomalous wind and thermal forcing alone. The difference between these two simulations gives an approximate estimate of the contribution from meltwater forcing alone to ongoing climate change. The forcing perturbations are derived using near-surface anomaly fields from observation-based JRA55-do v1.3 for the historical period (1991–2019), and CMIP6 projections for the 2020–2050 period, including wind forcing (10-m zonal wind velocity), thermal forcing (2-m air temperature and surface downwelling longwave radiation) and meltwater forcing (ice-sheet and ice-shelf melt). The parallel control experiment is carried out using the repeat-year forcing without any perturbation. The anomalies between concurrent periods of the perturbation and control experiments are then analysed to minimize the influence of model drift on our results, although it should be noted that model drift is small compared with the forced signal (Fig. 3a,b and Extended Data Fig. 3f). Properties analysed from the model simulations include the ocean temperature, salinity, potential density, and age, which corresponds to the volume-weighted time elapsed since any given water mass was last in contact with the atmosphere, revealing the ventilation rate of the deep and abyssal ocean. Further details about the model forcing are provided below.

The wind and thermal forcing perturbations are applied globally, with zonal-mean anomaly fields derived from two combined datasets: JRA55-do v1.3[32] for the historical period during 1991–2019, and the multi-model ensemble mean of CMIP6 models under a high-anthropogenic-emissions scenario, Shared Socioeconomic Pathway 5-8.5 (SSP5-8.5)[64], for the future climate component from 2020 until 2050. The resulting perturbation anomalies applied are shown in Extended Data Fig. 3a–c, with the list of CMIP6 models used indicated in the inset box. To remove interannual variability and abrupt transitions between the two forcing datasets (that is, historical reanalyses and projections) across 2019–2020, the anomaly fields are temporally smoothed with a third-degree polynomial function. By design, the forcing applied does not include any intrinsic interannual-to-decadal variability in atmospheric or meltwater variables, as our focus is on extracting the long-term forced signal. We also apply global zonal-mean anomaly fields of specific humidity to maintain constant relative humidity in the perturbation simulations.

The Antarctic and Greenland ice sheets have lost ice mass at an accelerating rate over recent periods between 1992–2011 and 2012–2017, from 119 ± 16 Gt yr^{-1} to 244 ± 28 Gt yr^{-1} in Greenland[10] and from 76 ± 59 Gt yr^{-1} to 219 ± 43 Gt yr^{-1} in Antarctica[9]. In our simulations for the period 2001–2050, the meltwater forcing perturbation is applied with a linear increase from 0 Sv to 0.009 Sv (about 284 Gt yr^{-1}) at a rate of 0.018 Sv per century around Greenland, and from 0 Sv to 0.080 Sv (about 2,523 Gt yr^{-1}) at a rate of 0.160 Sv per century around West Antarctica including the Weddell Sea and extending westwards to the Ross Sea. It is noted that the JRA55-do v1.3 model forcing[32] already includes the monthly climatology (1961–1990) of freshwater run-off from Greenland[65] and the time constant freshwater run-off from Antarctica derived from observational climatology[60], so that these meltwater anomalies represent recent and projected amplification in melt around the Antarctic and Greenland margins. The linear trend in applied meltwater rate anomalies is derived from the ice-sheet simulation of ref. [33]. During the historical period, forcing is constrained by satellite-based measurements, and during the projected period, using Representative Concentration Pathway 8.5 (RCP8.5) forcing.

We refer to our model experiments out to 2050 as projections, given that we employ CMIP6-derived projections of atmospheric property trends, alongside meltwater anomalies derived from ice-sheet projections, to force the coupled ocean–sea-ice model. However, there are some caveats in our experimental design. First, we impose the meltwater perturbation along the coast at the near surface, neglecting the spatial complexity owing to both the advection of icebergs away from the margin and the input of basal melt at depth. This is a common omission in previous simulations exploring the response to imposed meltwater forcing[13,16,17,53,66]. Although a portion of icebergs move fresh water away from the continent, the model's background ocean circulation at least helps advect the added meltwater along similar pathways to those travelled by icebergs[67]. In terms of basal melt, the meltwater released directly into the surface mixed layer in the model acts to stabilize the water column, whereas adding meltwater at depth would lead to upward convection of a buoyant plume into the surface mixed layer, taking

longer for this water to cap off convection at the surface, and leading to more dilution of the original meltwater anomaly. However, an added surface meltwater signal can also be advected away from the source locations more readily than subsurface meltwater, owing to more rapid surface ocean circulation than that found at depth. Initial tests with basal melt added at depth in our model suggest an even stronger slowdown in DSW formation than that simulated here. To properly incorporate basal melt and coupled ice-shelf–ocean feedbacks, an ice-shelf-cavity parameterization would be required, although such a parameterization would still have limitations due to uncertainties in the geometry of ice-shelf cavities and scarce observations[68], such that other biases would probably ensue[69].

To maintain an appropriate rate of meltwater increase in the model simulations as projected by ref. [33], an additional 20% meltwater anomaly is applied to compensate for the effect of the model surface salinity restoring fluxes. Even with this overshoot of meltwater anomaly applied, the effective Antarctic run-off simulated in the wind, thermal and meltwater forcing experiment is still underestimated by about 15% relative to the amount suggested by ref. [33]. Thus our estimates might be considered a lower bound on the response in a freely evolving model. The model-simulated freshening anomalies around Antarctica and Greenland during 2041–2050 are shown in Extended Data Fig. 3d,e, respectively.

The goal of our study is to assess the response of AABW formation and the abyssal ocean circulation to forcing anomalies resulting from future climate change. We therefore employ a high-resolution ocean–sea-ice model that has been shown to form and export AABW in a realistic manner. Focusing the computational workload on resolving the processes responsible for bottom water formation and abyssal ventilation ensures that changes in AABW are physically based. Although atmospheric feedbacks are not resolved in this framework, the feedback due to applied meltwater anomalies is only second order around the Antarctic margin. This can be seen by comparing fully coupled climate model projections with and without meltwater anomalies[25]. The coupled model analysed here is the ACCESS-ESM1.5 simulation, run under historical and then a future SSP5-8.5 scenario, with a meltwater anomaly applied over the twenty-first century based on ref. [33]. The analysis shown in Extended Data Fig. 4 uses the output from this meltwater case taken from ref. [25], only weighted by 85% to match the forcing magnitude applied in our study. In particular, our applied meltwater forcing is 1.70 Sv integrated over 2001–2050 compared with the total meltwater anomaly of 2.0 Sv accumulated over 2001–2050 in ref. [25]. This comparison reveals only a small impact of meltwater back onto atmospheric properties and circulation at southern mid- to high latitudes (Extended Data Fig. 4). In addition, the Antarctic sea-ice extent simulated in the wind and thermal plus meltwater forcing experiment closely matches observations[70], with both our forced experiments being an improvement in this regard compared with virtually all CMIP6 models, including the CMIP6 multi-model mean, which is biased low by about 2.5×10^6 km^2 (Extended Data Fig. 5a). Furthermore, the simulated sea-ice decline over 2001–2050 in our winds plus warming simulation (the configuration that most closely matches CMIP6 projections, as CMIP6 models do not include ice-sheet meltwater anomalies) is also comparable to that seen across both individual CMIP6 models as well as the CMIP6 multi-model mean, although CMIP6 models show a wide inter-model spread (Extended Data Fig. 5a). This inter-model spread is probably due to variations in the location and intensity of spurious open-ocean convection across CMIP6 models, which plays a significant role in setting sea-ice concentration at the surface. In terms of the model response to added meltwater, the Antarctic sea-ice extent anomaly we simulate is of the same overall tendency as that captured in the fully coupled ACCESS-ESM1.5 simulations, although the coupled model also includes a significant amount of internal variability (that is, the large interannual variations seen in Extended Data Fig. 5b). Any mismatch here between our forced model and the response of the fully coupled model, such as the overall stronger sea-ice response seen in the coupled model, is probably due to spurious open-ocean convection that is typical of coarse resolution models, which tends to impact sea-ice disproportionately (see, for example, ref. [71]).

We do not examine multiple ensemble members of the forced ocean–sea-ice model because without coupling to an atmospheric general circulation model, the ocean simulation is more deterministic, with intrinsic variability caused only by eddy variability and other ocean circulation transients. An indication of this can be seen when comparing the sea-ice response to added meltwater in the coupled and uncoupled experiments (Extended Data Fig. 5b), which reveals substantial intrinsic variability in the coupled mode, and only a slowly varying forced response in the uncoupled mode. Thus, multiple ensemble members are not required with our forced ocean–sea-ice approach. Indeed, the intrinsic overturning variability is only small compared with the forced signal in our experimental set-up, with the standard deviation of AABW transport and AMOC strength during 2001–2050 in the control run much less than the forced response (the standard deviation of AABW transport is 0.90 Sv, much less than the forced response of −7.0 Sv; the standard deviation of AMOC strength is 0.59 Sv, somewhat less than the forced response of −2.7 Sv; Fig. 3a,b). Again, this justifies our approach of a single ensemble member for each perturbation anomaly.

Surface water-mass transformation

The net surface water-mass transformation is calculated as the sum of heat and salt components offline based on monthly model output, using the method[43] below:

$$\Omega(\sigma, t) = \iint \left(\overbrace{\underbrace{\frac{\partial}{\partial\sigma}\frac{\partial\sigma}{\partial\theta}\dot{\theta}}_{\text{heat}} + \underbrace{\frac{\partial}{\partial\sigma}\frac{\partial\sigma}{\partial S}\dot{S}}_{\text{salt}}}^{\text{net}} \right) \mathrm{d}A, \tag{1}$$

where Ω is the transformation rate (Sv), σ is the potential density (kg m^{-3}), θ is the potential temperature (in K), S is the salinity and t is time. $\dot{\theta}$ and $\dot{S}$ represent the non-advective sources of surface heat flux (in K m s^{-1}) and freshwater flux (in m s^{-1}), respectively. Here A denotes the surface area integral polewards of the 1,000-m isobath on the Antarctic continental slope.

Heat and freshwater flux anomalies across 4,000 m

The heat (Q) and freshwater (F) flux anomalies across 4,000 m are calculated as

$$Q = \int_{4{,}000}^{\text{Bottom}} \rho c_p \frac{\mathrm{d}\theta}{\mathrm{d}t} \mathrm{d}z \tag{2}$$

and

$$F = \int_{4{,}000}^{\text{Bottom}} \frac{d}{\mathrm{d}t}\left(\frac{S_\mathrm{i}}{S_\mathrm{f}} - 1\right) \mathrm{d}z, \tag{3}$$

where θ is the potential temperature (in K), $\rho = 1{,}035$ kg m^{-3} is density, $c_p = 3{,}992.1$ J kg^{-1} K^{-1} is the specific heat capacity of seawater and dz is the vertical grid interval (m). Here S_i represents the climatological mean salinity and S_f is estimated as $S_\mathrm{f} = S_\mathrm{i} + \Delta S = S_i + \mathrm{d}S/\mathrm{d}t \times \Delta t$, by applying the linear trend of salinity expressed as dS/dt over an annual time period of Δt.

Our model simulations of the heat (Fig. 2a) and freshwater (Extended Data Fig. 9a) flux anomalies across 4,000 m over the historical period 1991–2010 agree well with observations (Fig. 8a in ref. [2] and Fig. 5b in ref. [3]). We further estimate that these freshwater flux anomalies are equivalent to freshwater additions of 6.44 Gt yr^{-1}, 2.85 Gt yr^{-1} and 0.53 Gt yr^{-1} into the Australian–Antarctic, Weddell–Enderby and Amundsen–Bellingshausen basins, respectively, of which the magnitude is within

the error bounds of observed estimates, apart from the Amundsen–Bellingshausen Basin (17 ± 13 Gt yr^{-1}, 10 ± 28 Gt yr^{-1} and 9 ± 4 Gt yr^{-1} between roughly 1991 and 2008 in observations; Table 1 in ref. [3]).

Decomposition of changes in water properties

The total change in water properties can be decomposed into two components: one owing to changes in isopycnal depth, referred to as 'heave', and the residual component owing to water-mass transformation. The water-mass transformation is based on the anomalous fields calculated in isopycnal coordinates and then transformed back to geopotential (z-level) surfaces. The difference between the properties in geopotential and isopycnal coordinates is approximated as the heave component.

Data availability

The ACCESS-OM2-01 model simulation output is stored on the Consortium for Ocean–Sea Ice Modeling in Australia (COSIMA) data collection website at https://doi.org/10.4225/41/5a2dc8543105a. The JRA55-do v1.3 data used to force the model simulations were obtained for the period 1991–2019 at https://climate.mri-jma.go.jp/~htsujino/jra55do.html. The CMIP6 data used to force the model simulations were obtained for the period 2020–2050 from the pangeo CMIP6 gallery at https://github.com/pangeo-gallery/cmip6. The specific additions for generating the model configurations used here can be provided upon request. The ACCESS-ESM1.5 model simulation output from ref. [25] was provided by A. Purich, and the datasets analysed in this study are publicly available in netCDF format at https://github.com/QianLi-Ocean/Antarctic_MWdriven_Abyssal_Circulation_Change/tree/main/Databases/ACCESS-ESM15. The observed sea-ice-extent data were retrieved from the National Snow and Ice Data Center (NSIDC) for the period 2001–2021 at https://doi.org/10.7265/N5K072F8.

Code availability

Model components are all open source. ACCESS-OM2 is available at https://github.com/COSIMA/access-om2/. The Jupyter notebooks used for the analyses described in this study are available in the GitHub repository at https://github.com/QianLi-Ocean/Antarctic_MWdriven_Abyssal_Circulation_Change.

55. Griffies, S. *Elements of the Modular Ocean Model (MOM): 2012 Release* Technical Report (NOAA/Geophysical Fluid Dynamics Laboratory, 2012).
56. Hunke, E. C., Lipscomb, W. H., Turner, A. K., Jeffery, N. & Elliott, S. *CICE: The Los Alamos Sea Ice Model Documentation and Software User's Manual Version 5.1* Technical Report (Los Alamos National Laboratory, 2015).
57. Large, W. G., McWilliams, J. C. & Doney, S. C. Oceanic vertical mixing: a review and a model with a nonlocal boundary layer parameterization. *Rev. Geophys.* **32**, 363–403 (1994).
58. Griffies, S. M. et al. Coordinated ocean–ice reference experiments (CORE). *Ocean Model.* **26**, 1–46 (2009).
59. Fox-Kemper, B., Ferrari, R. & Hallberg, R. Parameterization of mixed layer eddies. Part I: theory and diagnosis. *J. Phys. Oceanogr.* **38**, 1145–1165 (2008).
60. Depoorter, M. A. et al. Calving fluxes and basal melt rates of Antarctic ice shelves. *Nature* **502**, 89–92 (2013).
61. Simmons, H. L., Jayne, S. R., Laurent, L. C. & Weaver, A. J. Tidally driven mixing in a numerical model of the ocean general circulation. *Ocean Model.* **6**, 245–263 (2004).
62. Lee, H.-C., Rosati, A. & Spelman, M. J. Barotropic tidal mixing effects in a coupled climate model: oceanic conditions in the northern atlantic. *Ocean Model.* **11**, 464–477 (2006).
63. Stewart, K. et al. JRA55-do-based repeat year forcing datasets for driving ocean–sea-ice models. *Ocean Modelling* **147**, 101557 (2020).
64. O'Neill, B. C. et al. The Scenario Model Intercomparison Project (ScenarioMIP) for CMIP6. *Geosci. Model Dev.* **9**, 3461–3482 (2016).
65. Bamber, J., van den Broeke, M., Ettema, J., Lenaerts, J. & Rignot, E. Recent large increases in freshwater fluxes from Greenland into the North Atlantic. *Geophys. Res. Lett.* **39**, L19501 (2012).
66. Rye, C. D. et al. Antarctic glacial melt as a driver of recent Southern Ocean climate trends. *Geophys. Res. Lett.* **47**, e2019GL086892 (2020).
67. Stern, A. A., Adcroft, A. & Sergienko, O. The effects of Antarctic iceberg calving-size distribution in a global climate model. *J. Geophys. Res. Oceans* **121**, 5773–5788 (2016).
68. Mathiot, P., Jenkins, A., Harris, C. & Madec, G. Explicit representation and parametrised impacts of under ice shelf seas in the z* coordinate ocean model NEMO 3.6. *Geosci. Model Dev.* **10**, 2849–2874 (2017).
69. Naughten, K. A. et al. Future projections of Antarctic ice shelf melting based on CMIP5 scenarios. *J. Clim.* **31**, 5243–5261 (2018).
70. Fetterer, F., Knowles, K., Meier, W. N., Savoie, M. & Windnagel, A. K. Sea Ice Index, Version 3. *National Snow and Ice Data Center* https://doi.org/10.7265/N5K072F8 (2017).
71. Purich, A., England, M. H., Cai, W., Sullivan, A. & Durack, P. J. Impacts of broad-scale surface freshening of the Southern Ocean in a coupled climate model. *J. Clim.* **31**, 2613–2632 (2018).
72. Schmidtko, S., Heywood, K. J., Thompson, A. F. & Aoki, S. Multidecadal warming of Antarctic waters. *Science* **346**, 1227–1231 (2014).
73. Locarnini, R. A. et al. *World Ocean Atlas 2018, Volume 1: Temperature* Technical Report NOAA Atlas NESDIS 81 (NOAA, 2018); https://archimer.ifremer.fr/doc/00651/76338/.

Acknowledgements We thank members of the wider COSIMA community for collaborating with us to develop the ACCESS-OM2 model, and GFDL for providing the original MOM5 configuration on which the ACCESS-OM2 model is based; A. Purich for providing the processed CMIP6 data used to plot Extended Data Figs. 2a,c and 5a and the ACCESS-ESM1.5 model simulation output used to plot Extended Data Figs. 4 and 5b; and R. Holmes for suggesting the application of specific humidity anomalies in the perturbation simulations. This research was undertaken on the National Computational Infrastructure (NCI) in Canberra, Australia, which is supported by the Australian Government. M.H.E. and A.K.M. are supported by the ARC Australian Centre for Excellence in Antarctic Science (ACEAS; ARC Grant No. SR200100008). Q.L. is supported by the NASA MAP programme 19-MAP19-0011 and the MIT-GISS cooperative agreement. M.H.E., A.M.H. and A.K.M. were also supported by Australian Research Council (ARC) Discovery Project DP190100494, and A.K.M. by ARC DECRA Fellowship DE170100184.

Author contributions M.H.E. conceived the study and along with A.M.H. and Q.L. designed the model experiments. Q.L. undertook the model simulations and produced the analyses with input from all authors. M.H.E. and Q.L. led the revisions of the original submitted manuscript. All authors contributed to the development of ideas, analysis, writing and refinement of the paper.

Competing interests The authors declare no competing interests.

Additional information

Correspondence and requests for materials should be addressed to Matthew H. England.

Peer review information *Nature* thanks the anonymous reviewers for their contribution to the peer review of this work.

Reprints and permissions information is available at http://www.nature.com/reprints.

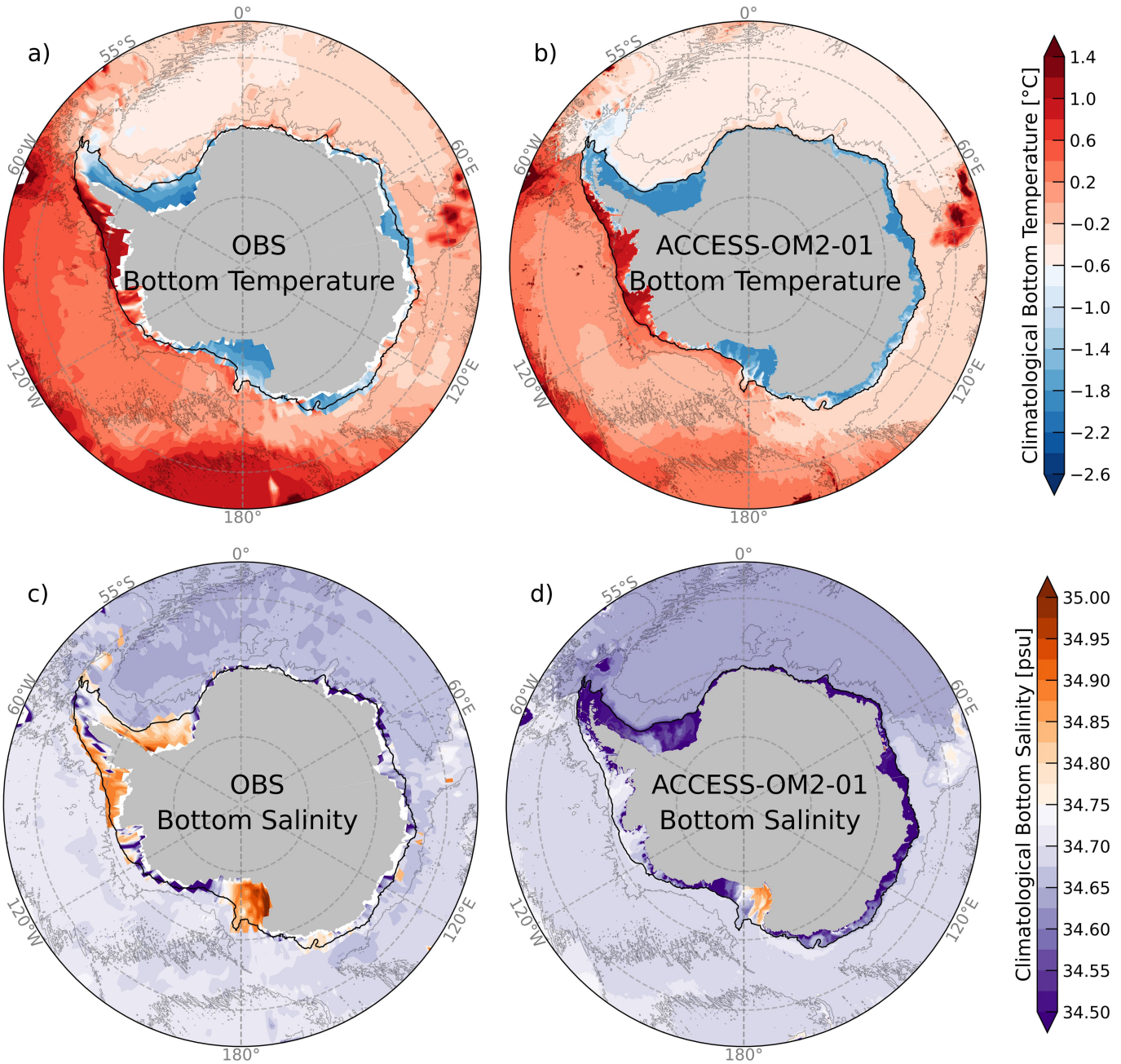

Extended Data Fig. 1 | Observed and modelled abyssal ocean temperature and salinity. Bottom **a**) temperature (°C) and **c**) salinity (psu) from the observational climatological mean on the continental shelf over 1975–2012 based on ref. [72] and in the abyss over 1955–2017 based on the World Ocean Atlas 2018[73]) and the equivalent **b**) temperature (°C) and **d**) salinity (psu) values in the ACCESS-OM2-01 control run after a 200 year spin-up. All temperatures and salinities shown correspond to the bottom-most value in both observations and the model. Grey contours represent the 4000 m isobath, and the black line denotes the 1000 m isobath around the Antarctic margin.

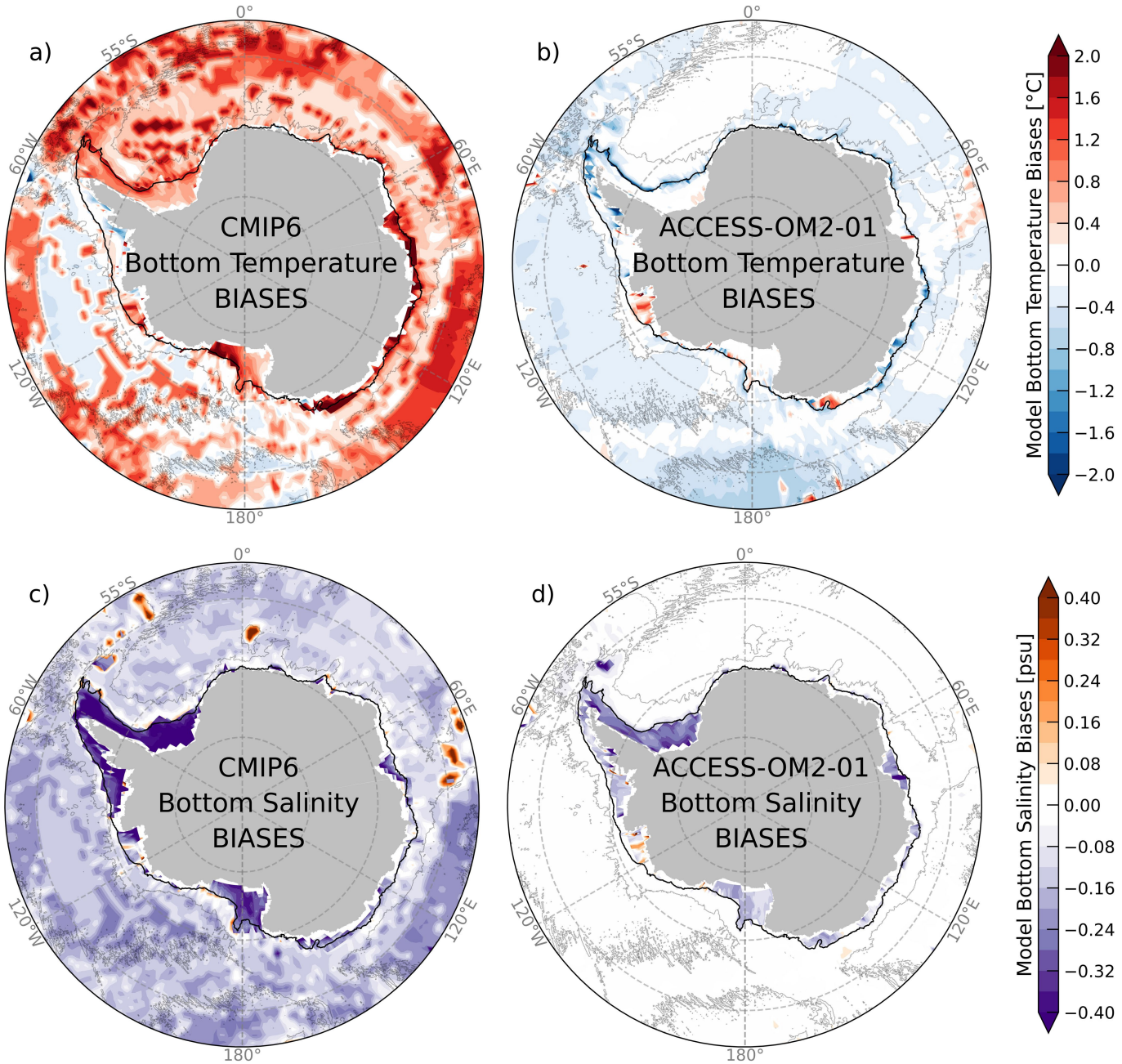

Extended Data Fig. 2 | Model abyssal ocean temperature and salinity evaluation. Model bottom **a**, **c**) temperature (°C) and **b**, **d**) salinity (psu) biases relative to observations in the multi-model ensemble mean of CMIP6 models[5] during the historical period 1975–2012 and from the baseline ACCESS-OM2-01 control run, respectively. Grey contours represent the 4000 m isobath, and the black line denotes the 1000 m isobath around the Antarctic margin. Note that individual CMIP6 model biases in abyssal temperature and salinity are generally much larger than the biases seen in the multi-model mean[5].

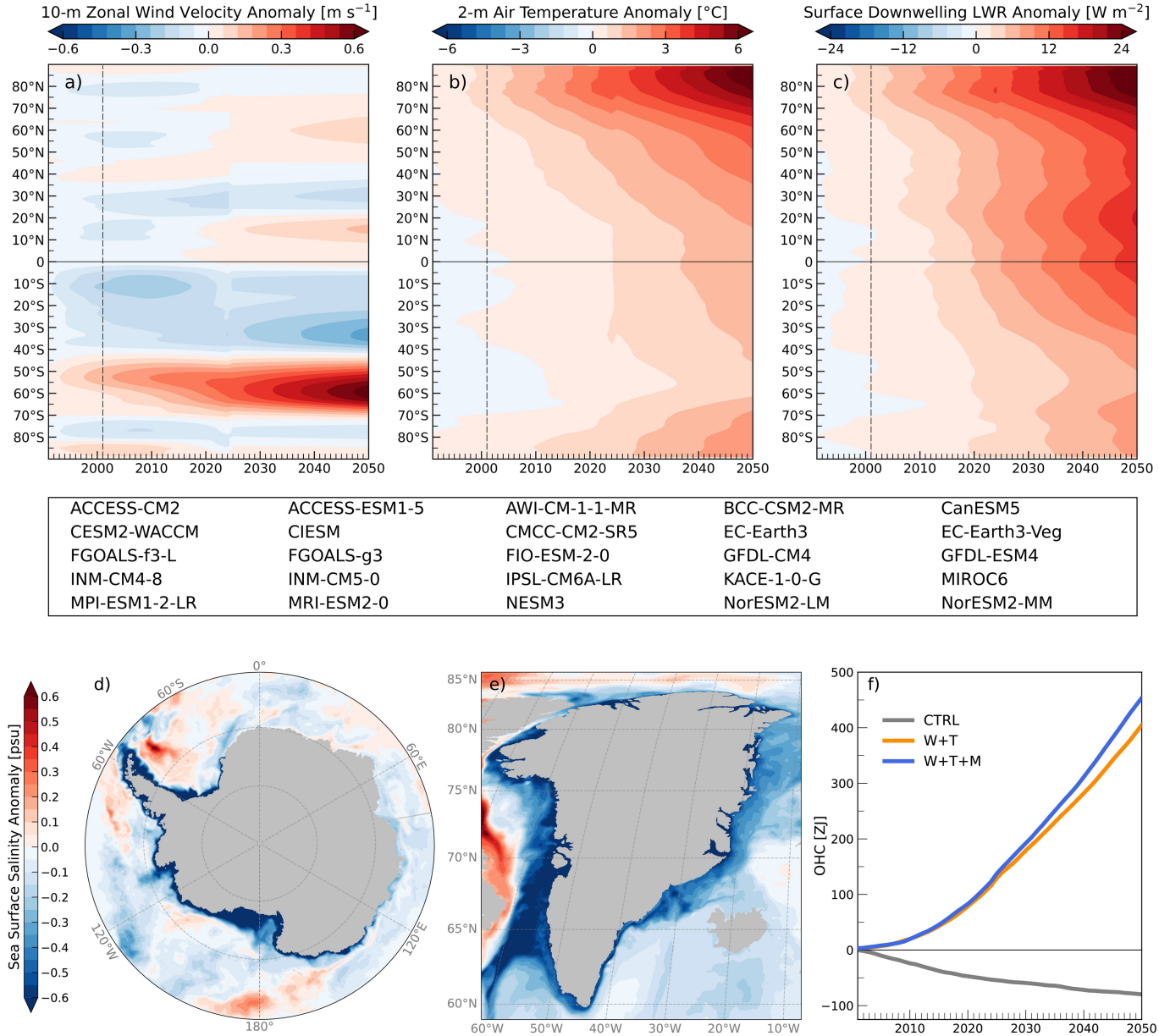

Extended Data Fig. 3 | Model forcing fields for wind, thermal and meltwater perturbations. Hovmöller diagram of zonal-mean **a**) 10-m zonal wind velocity anomaly (m s^{-1}), **b**) 2-m air temperature anomaly (°C) and **c**) surface downwelling longwave radiation anomaly (W m^{-2}), from observation-based JRA55-do v1.3 for the historical period 1991–2019 and CMIP6 for the future period 2020–2050 (Methods). These required forcing fields for our simulations were derived using the multi-model mean of all 25 CMIP6 models available at the time of setting up the experiments (listed in the inset box). Sea surface salinity anomaly (psu) during 2041–2050 from the [wind+thermal+meltwater] experiment relative to the control run, around **d**) Antarctica and **e**) Greenland, respectively. **f**) Time series of annual-mean globally integrated Ocean Heat Content (OHC) relative to 2001 (ZJ = 10^{21} J) from the control run (grey line), the [wind+thermal] run (orange line) and the [wind+thermal+meltwater] run (blue line), respectively.

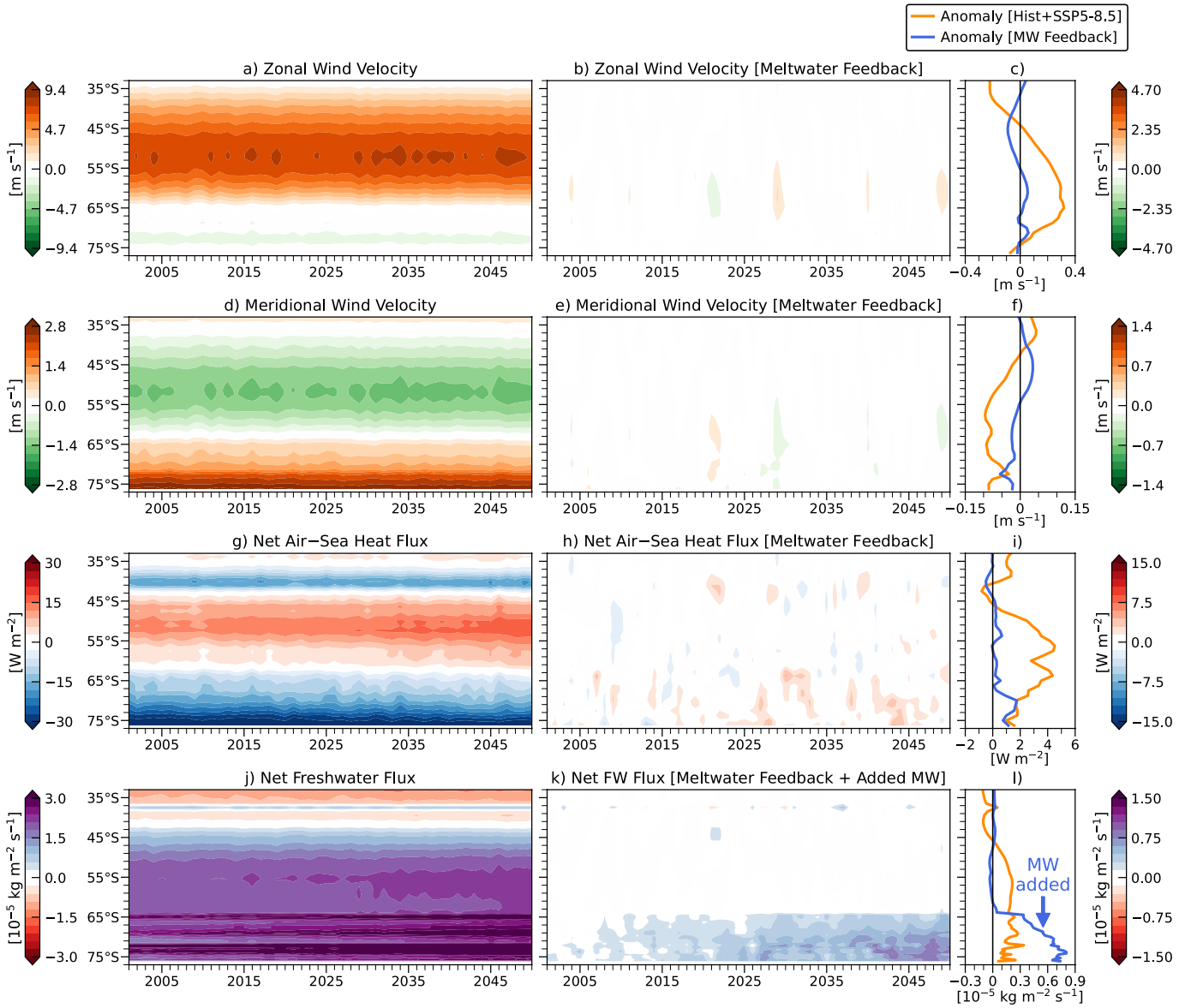

Extended Data Fig. 4 | Meltwater-driven air-sea feedback evaluation. Hovmöller diagrams of zonal-mean surface forcing, shown as total (left panel) and estimated meltwater feedback (middle panel) for **a**,**b**) zonal wind velocity (m s^{-1}), **d**,**e**) meridional wind velocity (m s^{-1}), **g**,**h**) net air-sea heat flux (W m^{-2}) and **j**,**k**) net freshwater flux (kg m^{-2} s^{-1}) during 2001–2050 from the fully coupled ACCESS-ESM1.5 run with added meltwater. The meltwater feedback is estimated from the difference between fully coupled model runs with and without meltwater, based on simulations run under historical and SSP5-8.5 forcing. To match the meltwater amount we apply, the coupled model output from ref. [25] is weighted by 85% (as detailed in Methods). The *total* field is the sum of that simulated in the run under historical and SSP5-8.5 forcing, plus the weighted anomaly driven by the meltwater component. The far right hand panels show the 2041–2050-mean *anomaly* of **c**) zonal wind velocity (m s^{-1}), **f**) meridional wind velocity (m s^{-1}), **i**) net air-sea heat flux (W m^{-2}) and **l**) net freshwater flux (kg m^{-2} s^{-1}) driven by the meltwater component (blue lines) vs. anomalies due to climate change forcing without meltwater (orange lines), calculated relative to the 2001–2010-mean. The net heat flux comprises the sum of shortwave radiation, longwave radiation, latent and sensible heat fluxes. The net freshwater flux comprises precipitation, evaporation and run-off (including extra meltwater input where applied; i.e., in panel (l)). Heat and freshwater fluxes are defined positive from the atmosphere into the ocean. Zonal means are calculated over ocean grid boxes only (i.e. not over land).

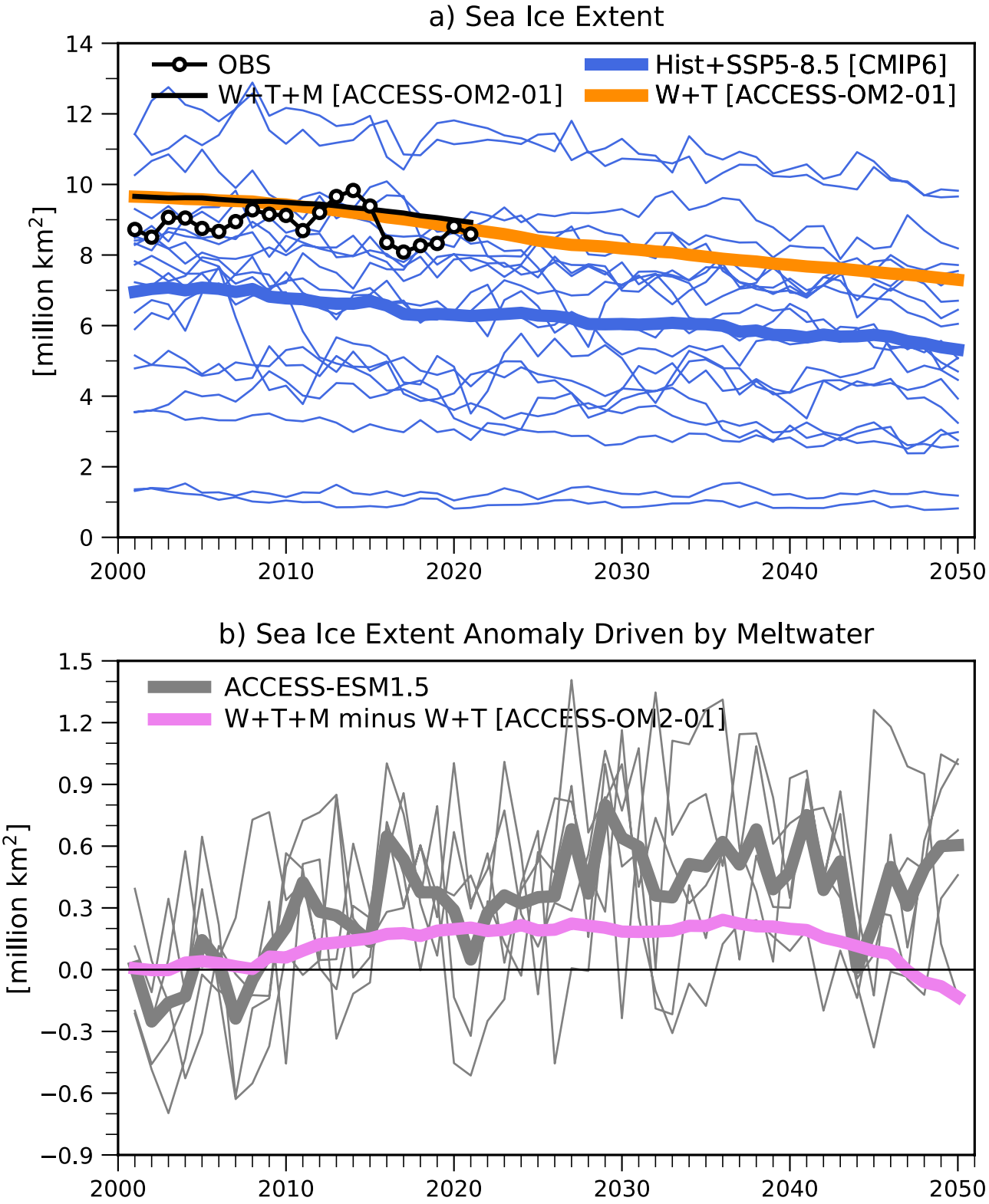

Extended Data Fig. 5 | Model Antarctic sea-ice extent evaluation. a) Time series of annual-mean sea-ice extent (million km^2) from observations[70] (black line with hollow circles), the [wind+thermal+meltwater] run (black line) during 2001–2021, the [wind+thermal] run (orange line), and the CMIP6 model simulations[24] under historical and SSP5-8.5 forcing (thin blue lines) during 2001–2050. The sea-ice extent is defined as the area covered by ice with a concentration of at least 15%. The thick blue line is the CMIP6 multi-model mean. The decline rate of sea-ice extent from the [wind+thermal] run (−0.53 million km^2 per decade; orange line) lies within the range of CMIP6 models (−0.34 ± 0.2 million km^2 per decade). **b**) Time series of the response in annual-mean sea-ice extent (million km^2) to an equivalent meltwater anomaly in the [wind+thermal+meltwater] run (violet line), and from the fully coupled ACCESS-ESM1.5 run during 2001–2050, shown as an ensemble mean (thick grey line) and as individual members (thin grey lines).

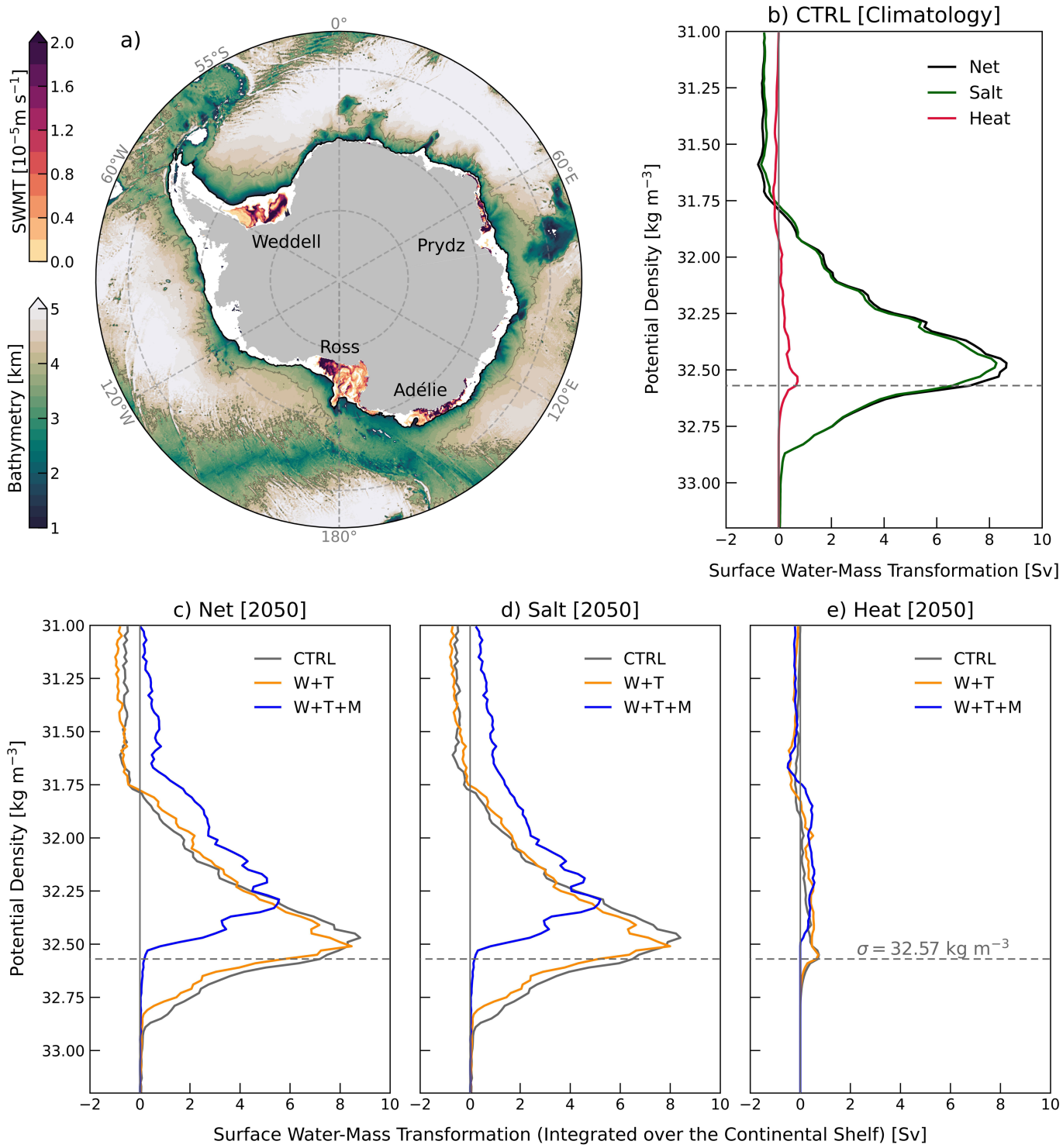

Extended Data Fig. 6 | Control and projected Dense Shelf Water formation changes in 2050. a) Surface water-mass transformation (on the continental shelf; 10^{-5} m s^{-1}) and bathymetry (in the abyss; km) from the control run. Surface water-mass transformation integrated over the Antarctic continental shelf area (poleward of the 1000 m isobath; Sv) for the net, salt and heat components **b**) in climatology from the control run and **c**,**d**,**e**) in 2050 from the control run, the [wind+thermal] run and the [wind+thermal+meltwater] run. Dashed line in **b**,**c**,**d**,**e**) denotes the 32.57 kg m^{-3} isopycnal (referenced to 1000 m), across which the most significant reduction in water-mass transformation in 2050 for the [wind+thermal+meltwater] run is evident. The surface water-mass transformation rate in a) is also computed across this potential density layer.

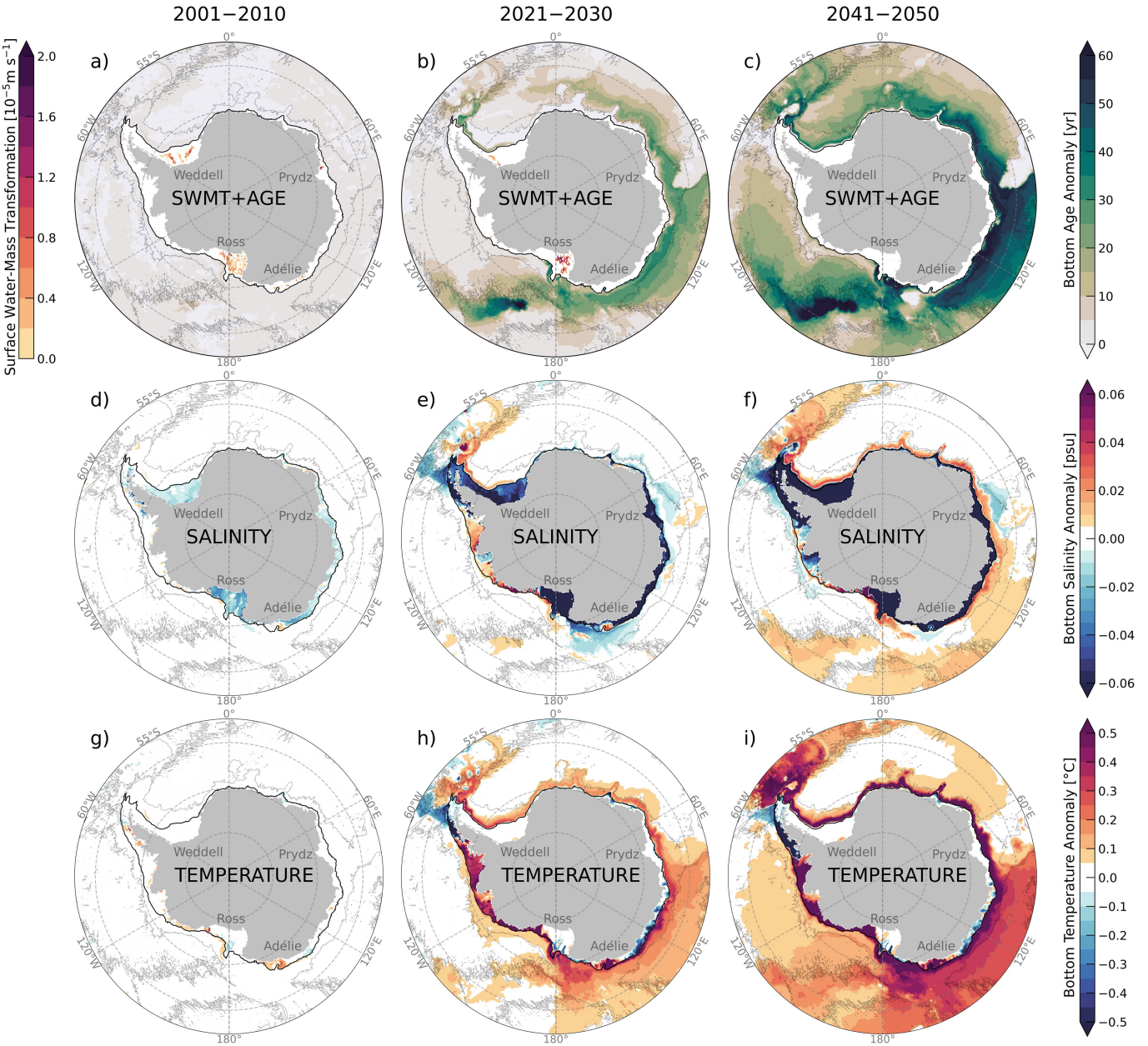

Extended Data Fig. 7 | Recent and projected bottom water property changes due to the meltwater anomalies. a–**c**) Surface water-mass transformation (on the continental shelf; 10^{-5} m s^{-1}) and bottom seawater age anomaly (in the abyss; years), **d**–**f**) bottom salinity anomaly (psu) and **g**–**i**) bottom temperature anomaly (°C) from the meltwater component during the decades 2001–2010, 2021–2030 and 2041–2050, respectively, relative to the control run. Grey contours represent the 4000 m isobath, and the black line denotes the 1000 m isobath around the Antarctic margin. The surface water-mass transformation rate is computed across the 32.57 kg m^{-3} isopycnal (referenced to 1000 m), across which the SWMT shows the most significant reduction.

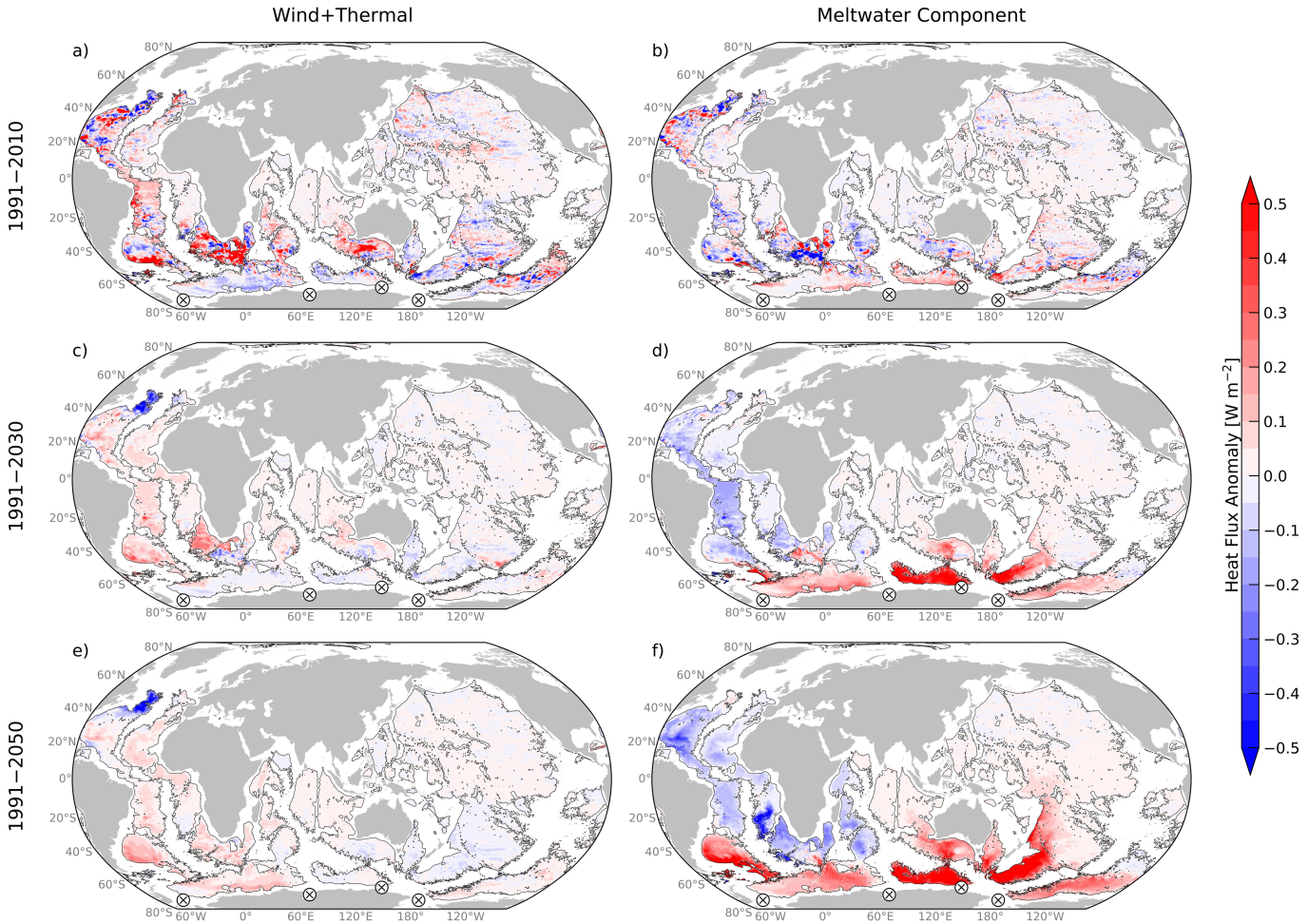

Extended Data Fig. 8 | Recent and projected abyssal warming trends from the [wind+thermal] run and the estimated meltwater component. Warming is shown as the heat flux anomaly (W m^{-2}) across 4000 m implied by the warming below 4000 m during the period a,b) 1991–2010, c,d) 1991–2030 and e,f) 1991–2050 from the [wind+thermal] run and the meltwater component, respectively. Grey contours represent the 4000 m isobath. The four arrow tail symbols along the coast of Antarctica denote the key locations of DSW and AABW formation.

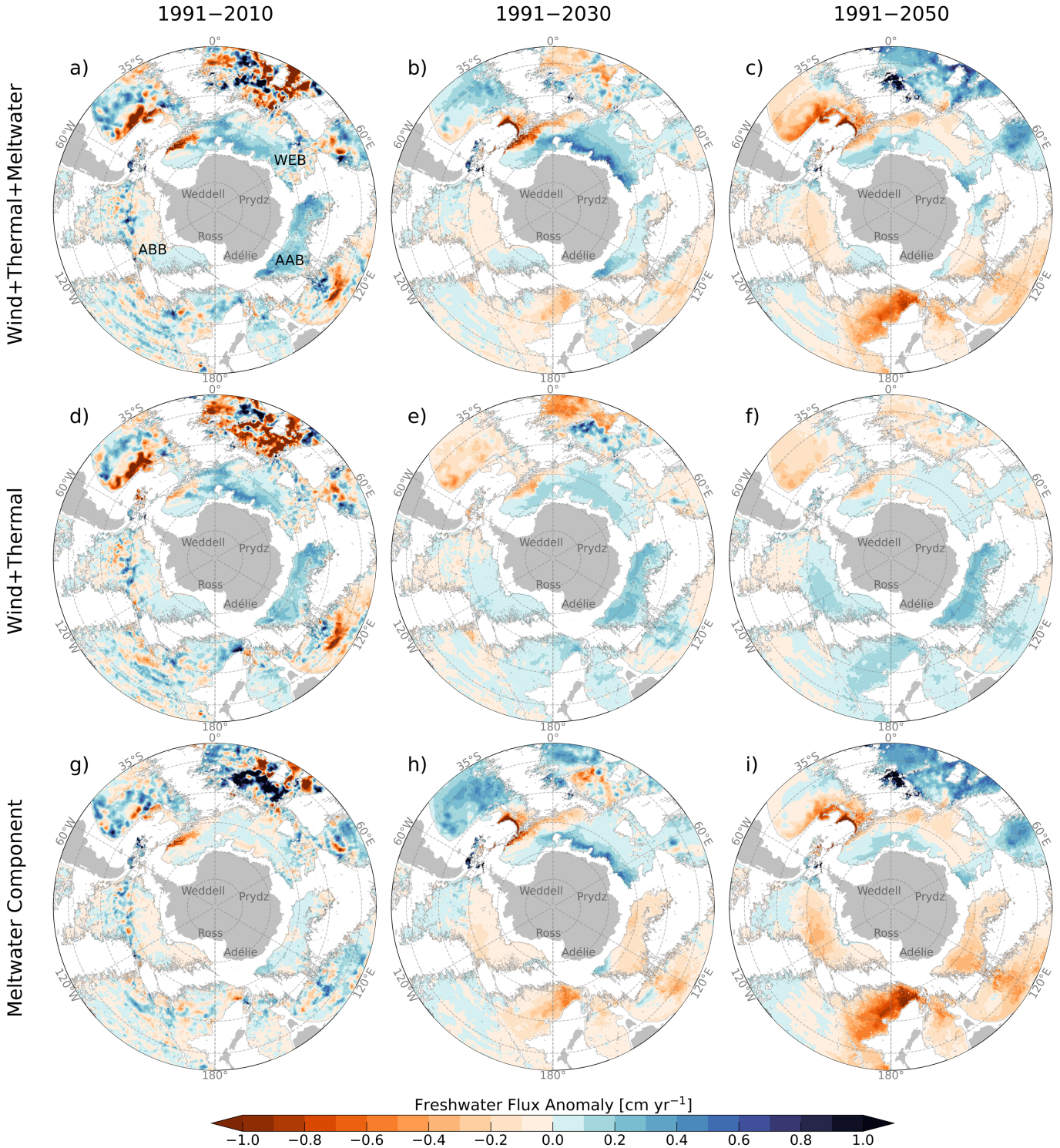

Extended Data Fig. 9 | Recent and projected abyssal freshening. Freshwater flux anomaly (cm yr^{-1}) across 4000 m during the period **a**,**d**,**g**) 1991–2010, **b**,**e**,**h**) 1991–2030 and **c**,**f**,**i**) 1991–2050 from the [wind+thermal+meltwater] run, the [wind+thermal] run and the estimated meltwater component, respectively. Grey contours represent the 4000 m isobath. The Australian–Antarctic basin (AAB), Weddell–Enderby basin (WEB) and Amundsen–Bellingshausen basin (ABB) are indicated in a).

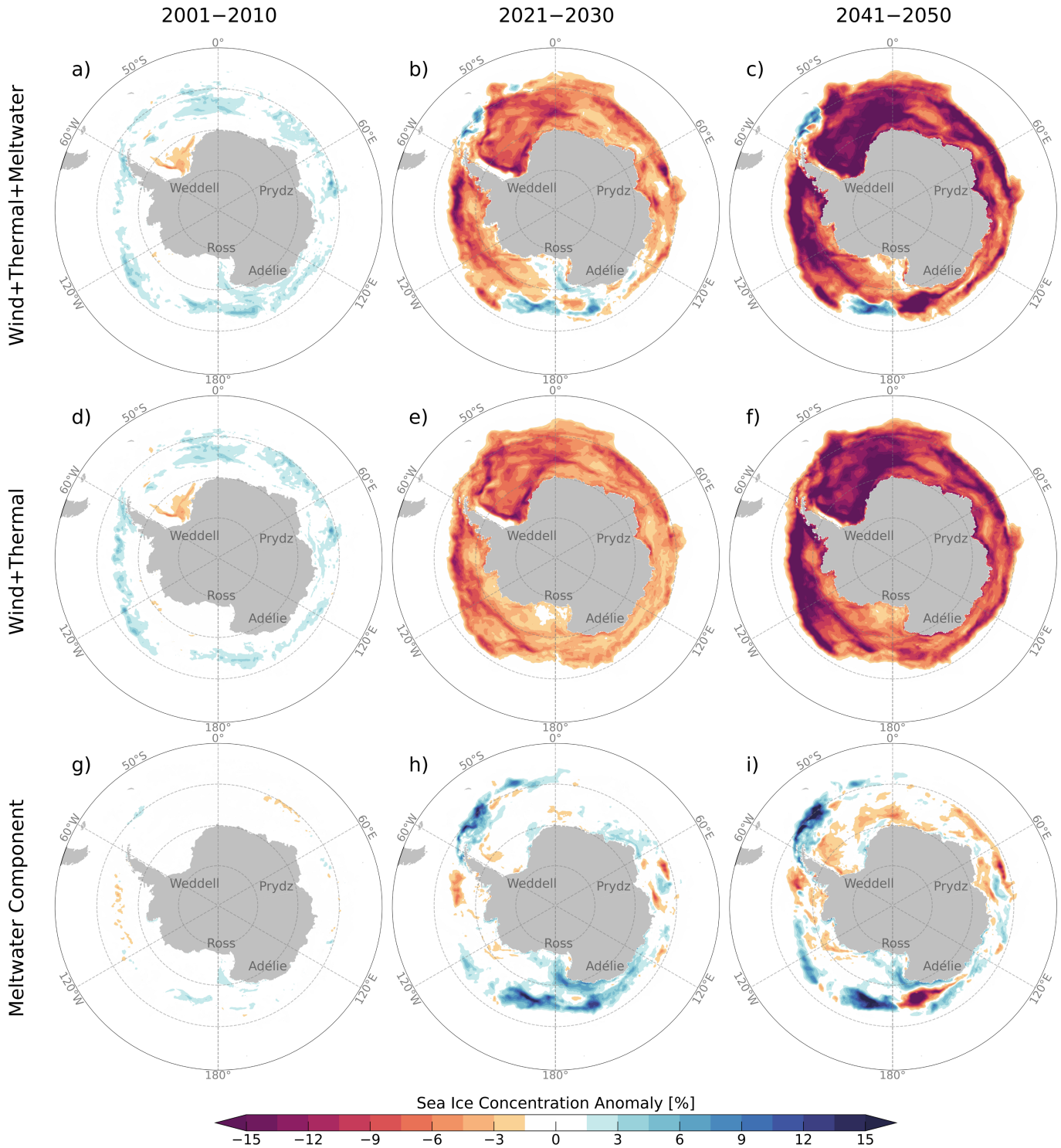

Extended Data Fig. 10 | Recent and projected sea-ice changes. Sea-ice concentration anomaly (%) during the decade **a**,**d**,**g**) 2001–2010, **b**,**e**,**h**) 2021–2030 and **c**,**f**,**i**) 2041–2050 from the [wind+thermal+meltwater] run, the [wind+thermal] run and the estimated meltwater component, respectively. Positive and negative values indicate sea-ice growth and decline, respectively.

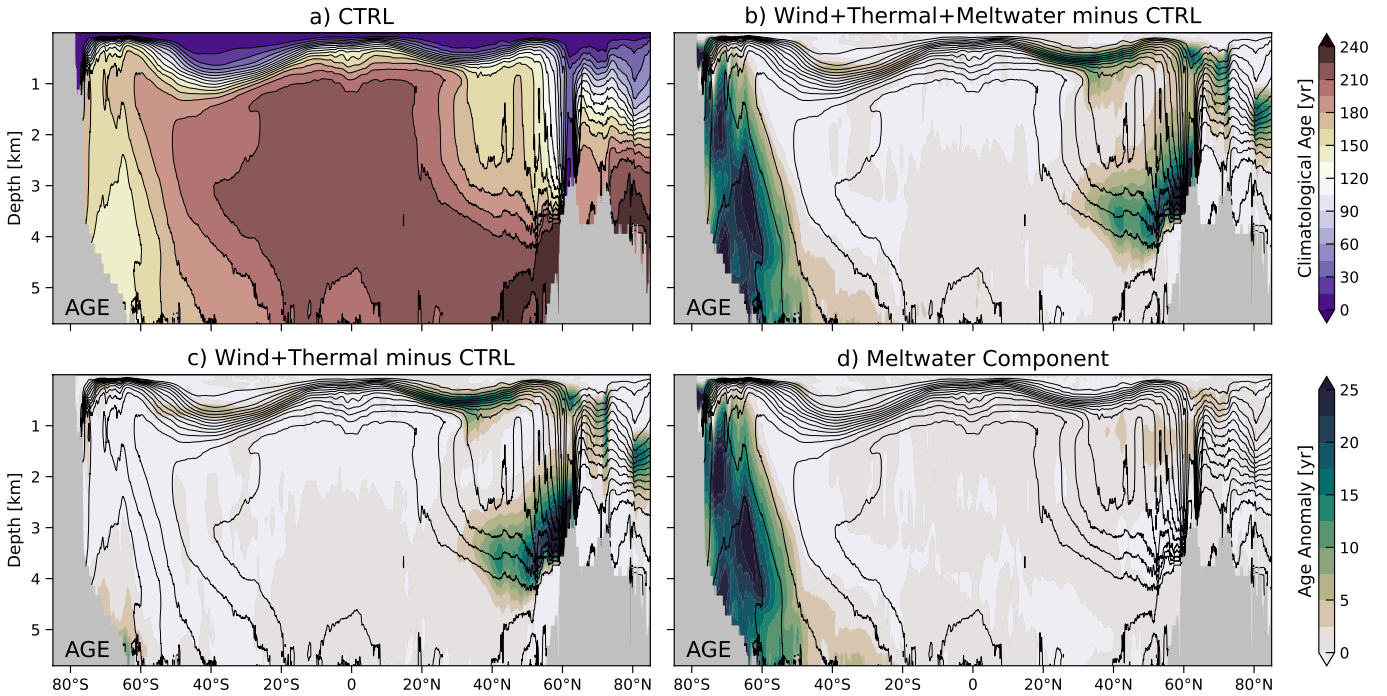

Extended Data Fig. 11 | Projected global seawater age changes during 2041–2050. Vertical cross-sections of zonal-mean **a**) climatological mean seawater age (years) from the control run, and **b**,**c**,**d**) seawater age anomaly (years) during 2041–2050 from the [wind+thermal+meltwater] run, the [wind+thermal] run and the estimated meltwater component, respectively. Contours represent the climatological mean seawater age with an interval of 15 years.

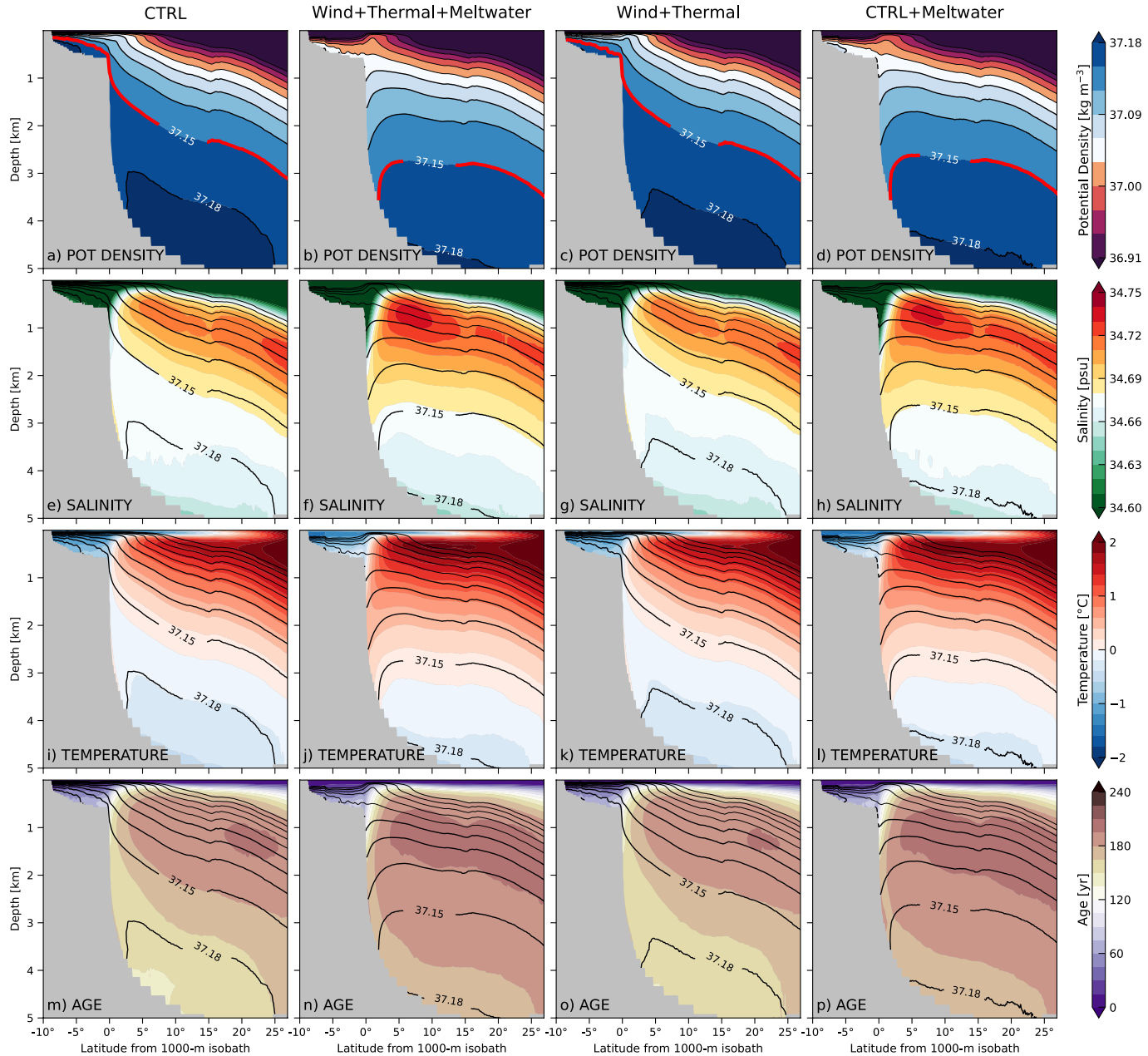

Extended Data Fig. 12 | Projected Southern Ocean water-mass properties in 2041–2050. Vertical cross-sections of zonal-mean **a**–**d**) potential density (kg m^{-3}), **e**–**h**) salinity (psu), i-l) temperature (°C) and m-p) seawater age (years) during 2041–2050 from the control run, the [wind+thermal+meltwater] run, the [wind+thermal] run and the estimated meltwater component, respectively. The far right hand panels show the sum of the mean properties from the control run and the estimated meltwater contribution. Contours show the corresponding potential density (referenced to 2000 m) during 2041–2050, ranging from 36.91 kg m^{-3} to 37.18 kg m^{-3} with an interval of 0.03 kg m^{-3}. Latitude is shown relative to the 1000 m isobath.

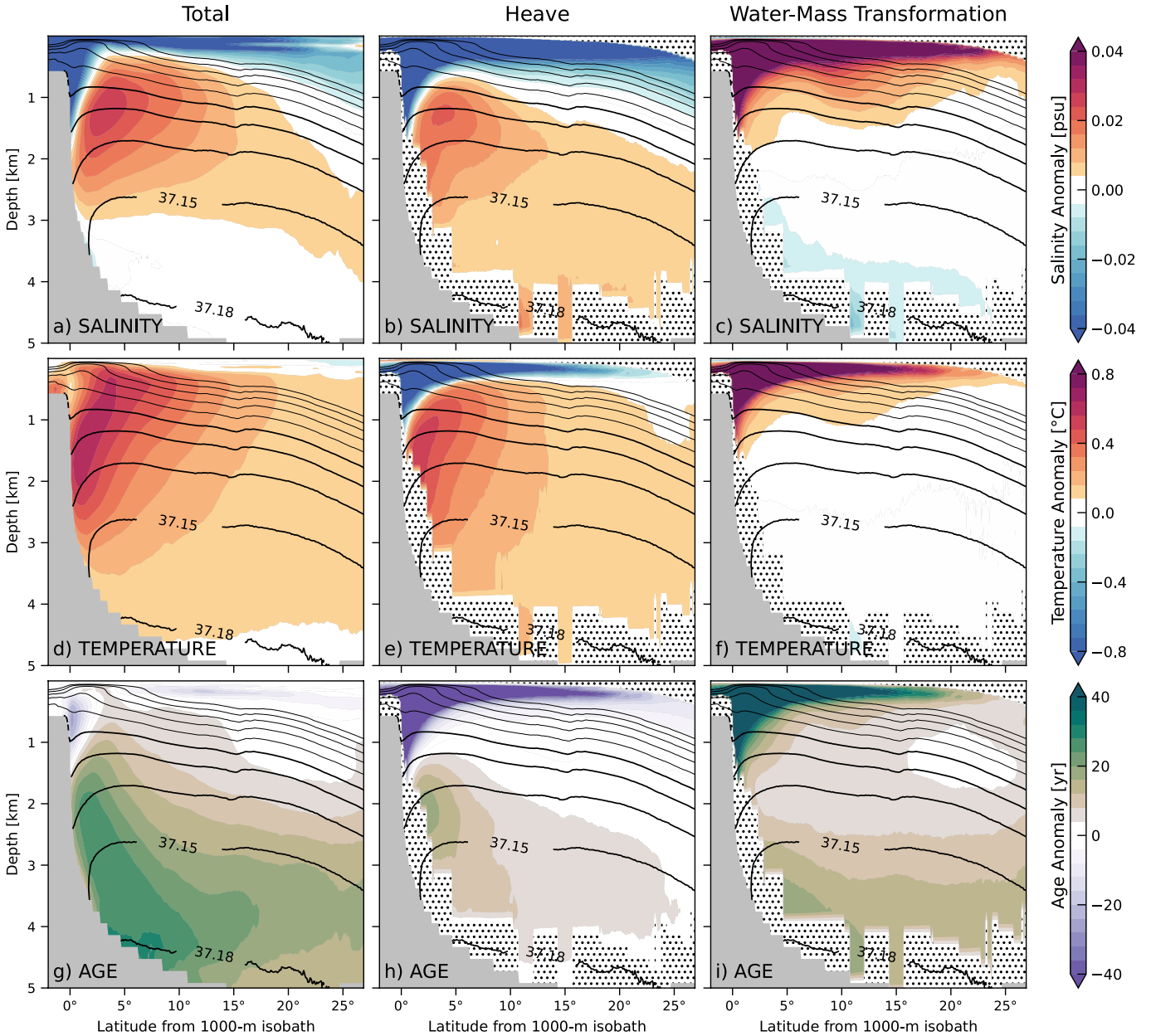

Extended Data Fig. 13 | Decomposition of projected meltwater-driven water-mass changes during 2041–2050. Vertical cross-sections of zonal-mean **a**–**c**) salinity anomaly (psu), **d**–**f**) temperature anomaly (°C) and **g**–**i**) seawater age anomaly (years) during 2041–2050 estimated for the meltwater component of the total change, heave component and residual component due to water-mass transformation (i.e. once heave is removed), respectively (Methods). Contours show the corresponding potential density (referenced to 2000 m) during 2041–2050, ranging from 36.91 kg m^{-3} to 37.18 kg m^{-3} with an interval of 0.03 kg m^{-3}. Latitude is shown relative to the 1000 m isobath. Stippling indicates missing values due to transforming the vertical coordinates between depth and density values.